CrossMark

J. Fluid Mech. (2023), *vol*. 966, A2, doi:10.1017/jfm.2023.412

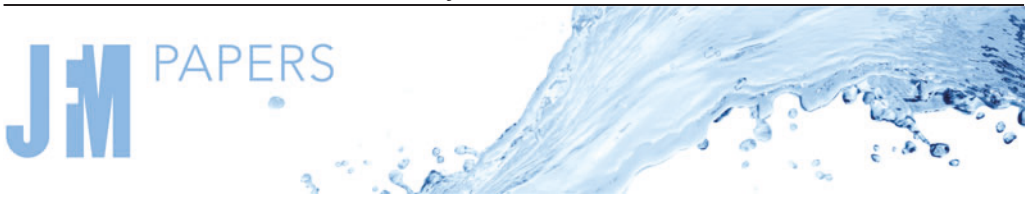

The effects of boundary proximity on Kelvin–Helmholtz instability and turbulence

Chih-Lun Liu[1],†, **Alexis K. Kaminski**[2] **and William D. Smyth**[1]

[1]College of Earth, Ocean and Atmospheric Sciences, Oregon State University, Corvallis, OR 97331, USA

[2]Department of Mechanical Engineering, University of California, Berkeley, Berkeley, CA 94720, USA

(Received 23 December 2022; revised 11 May 2023; accepted 17 May 2023)

Studies of Kelvin–Helmholtz (KH) instability have typically modelled the initial flow as an isolated shear layer. In geophysical cases, however, the instability often occurs near boundaries and may therefore be influenced by boundary proximity effects. Ensembles of direct numerical simulations are conducted to understand the effect of boundary proximity on the evolution of the instability and the resulting turbulence. Ensemble averages are used to reduce sensitivity to small variations in initial conditions. Both the transition to turbulence and the resulting turbulent mixing are modified when the shear layer is near a boundary: the time scales for the onset of instability and turbulence are longer, and the height of the KH billow is reduced. Subharmonic instability is suppressed by the boundary because phase lock is prevented due to the diverging phase speeds of the KH and subharmonic modes. In addition, the disruptive influence of three-dimensional secondary instabilities on pairing is more profound as the two events coincide more closely. When the shear layer is far from the boundary, the shear-aligned convective instability is dominant; however, secondary central-core instability takes over when the shear layer is close to the boundary, providing an alternate route for the transition to turbulence. Both the efficiency of the resulting mixing and the turbulent diffusivity are dramatically reduced by boundary proximity effects.

Key words: shear-flow instability, turbulent mixing, shear layer turbulence

1. Introduction

Turbulent mixing plays a crucial role in the vertical exchange of heat, momentum, nutrients and carbon in the ocean (Wunsch & Ferrari 2004). The performance of large-scale ocean and climate models depends on the parameterization of small-scale mixing and

† Email address for correspondence: liuchihl@oregonstate.edu

© The Author(s), 2023. Published by Cambridge University Press. This is an Open Access article, distributed under the terms of the Creative Commons Attribution licence (http://creativecommons.org/licenses/by/4.0), which permits unrestricted re-use, distribution and reproduction, provided the original article is properly cited.

https://doi.org/10.1017/jfm.2023.412 Published online by Cambridge University Press

turbulent fluxes. Turbulent mixing is often modelled by the classical Kelvin–Helmholtz (KH) instability of a stably stratified shear layer (e.g. Smyth & Carpenter 2019). The shear layer rolls up to form a periodic train of 'billow' structures which subsequently break down via three-dimensional (3-D) secondary instabilities (Mashayek & Peltier 2012*a*,*b*), leading to turbulence and vertical transport.

Turbulence in stratified shear flows has been observed in a variety of fluid environments, ranging from diurnal warm layers near the surface ocean (Hughes *et al.* 2021), equatorial undercurrents (Moum, Nash & Smyth 2011), seamounts and oceanic ridges (Chang, Jheng & Lien 2016; Chang *et al.* 2022), estuarine shear zones (Geyer *et al.* 2010; Holleman, Geyer & Ralston 2016; Tu *et al.* 2022) and the abyssal ocean (Van Haren & Gostiaux 2010; Van Haren *et al.* 2014) to canopy waves above forests (Mayor 2017; Smyth, Mayor & Lian 2023) and higher atmospheric layers (Fukao *et al.* 2011). Theoretical understanding has been greatly advanced via the use of direct numerical simulations (Caulfield & Peltier 2000; Smyth & Moum 2000; Mashayek & Peltier 2011, 2012*a*,*b*; Salehipour, Peltier & Mashayek 2015; Kaminski & Smyth 2019; Lewin & Caulfield 2021; VanDine, Pham & Sarkar 2021). However, most theoretical studies have assumed that the shear layer is located far from any boundary. In geophysical flows, much of the most important mixing is found in complex boundary regions (Munk & Wunch 1998; Wunsch & Ferrari 2004; Smyth *et al.* 2023); therefore, a comprehensive understanding of boundary effects on sheared, stratified turbulence is critical for the prediction of such mixing events.

This article describes the impact of proximity to a no-slip boundary on KH instability and its secondary instabilities as well as the resulting turbulent mixing. We seek to understand how the boundary modifies the route to turbulence and the ensuing turbulence characteristics, e.g. mixing efficiency. In the process, we identify and explore a novel mechanism for the suppression of pairing and turbulence by boundary effects.

Subharmonic pairing, wherein adjacent KH billows merge (Corcos & Sherman 1976; Klaassen & Peltier 1989; Smyth & Peltier 1993), leads to upscale energy cascade and may increase turbulent mixing (Rahmani, Lawrence & Seymour 2014) by raising the available potential energy. This mechanism is sensitive to the details of the initial conditions. For example, Dong *et al.* (2019) showed how the initial phase difference between the primary KH and the subharmonic Fourier components leads to a significant difference in mixing characteristics. Guha & Rahmani (2019) predicted the strength and pattern of pairing in terms of the initial asymmetry between consecutive wavelengths of the vertical velocity profile.

The 3-D secondary instabilities initiate a downscale energy cascade and catalyze the transition to turbulence (Klaassen & Peltier 1985*a*; Mashayek & Peltier 2012*a*,*b*). Mashayek & Peltier (2013) showed that pairing can be suppressed, at high Reynolds number, by the early emergence of various 3-D secondary instabilities. This provides one explanation for the fact that pairing is observed rarely, if ever, in geophysical flows (although see Armi & Mayr 2011). Here, we propose an alternative mechanism whereby pairing instability is suppressed by the boundary.

Turbulent mixing in stratified fluids is often parameterized using mixing efficiency, η, a ratio of the irreversible mixing to the rate at which the kinetic energy is irreversibly lost to viscosity. A canonical constant value of $\Gamma = \eta/(1-\eta) = 0.2$ ($\eta = 1/6$), known as the flux coefficient, is often assumed in the parameterization of the eddy diffusivity, $K_\rho = \Gamma\epsilon'/N^2$ (Osborn 1980), where ϵ' is the viscous dissipation rate of turbulent kinetic energy, and N is the buoyancy frequency. However, previous studies have shown that mixing efficiency is not necessarily constant (Ivey, Winters & Koseff 2008; Gregg *et al.* 2018; Caulfield 2021). Here, our goal is to understand the effect of boundary proximity on turbulent mixing and its efficiency.

https://doi.org/10.1017/jfm.2023.412 Published online by Cambridge University Press

We study these phenomena by comparing statistics from ensembles of direct numerical simulations in which the initial state is varied slightly and randomly. This is done using ensembles of direct numerical simulations (DNS), where initial perturbations are varied due to the sensitive dependence on initial conditions (Liu, Kaminski & Smyth 2022). Liu *et al.* (2022) showed that a small change in the initial random perturbation can lead to a substantial variation in the timing and strength of turbulence. This variation results from the interactions between mean flow, primary KH, subharmonic and various 3-D secondary instabilities.

The paper is organized as follows. In § 2 we describe the set-up for our numerical simulations and the choice of the initial parameter values as well as the diagnostic tools required for the analysis of energetics and mixing. We then describe the boundary effects on primary KH instability in § 3, and show that the evolution of KH instability depends strongly on boundary proximity. In § 4 we explain how the boundary suppresses pairing by altering the phase speeds of the KH and subharmonic modes. Boundary effects on 3-D secondary instabilities are presented in § 5. In § 5.4, we show how boundary proximity modifies the competition between the subharmonic instability and turbulence. In § 6, we describe the boundary effects on the irreversible mixing, mixing efficiency and turbulent diffusivity. Conclusions are summarized in § 7.

2. Methodology

2.1. *The mathematical model*

We begin by considering a stably stratified parallel shear layer

$$U^*(z) = U_0^* \tanh\left(\frac{z^*}{h^*} + \frac{L_z^*/2 - d^*}{h^*}\right) \quad \text{and} \quad B^*(z) = B_0^* \tanh\left(\frac{z^*}{h^*} + \frac{L_z^*/2 - d^*}{h^*}\right), \tag{2.1a,b}$$

in which $2U_0^*$ and $2B_0^*$ are, respectively, velocity and buoyancy differences across the shear layer and $2h^*$ is its thickness (figure 1). Asterisks indicate dimensional quantities. The stratified shear layer has a distance d^* from the lower boundary. The domain has a vertical extent L_z^*. The Cartesian coordinates are x^* (streamwise), y^* (spanwise) and z^* (vertical, positive upwards). The non-dimensional velocity and buoyancy profiles become

$$U(z) = B(z) = \tanh\left(z + \frac{L_z}{2} - d\right), \tag{2.2}$$

after non-dimensionalizing velocities by U_0^*, buoyancy by B_0^*, lengths by h^* and times by the advective time scale h^*/U_0^*.

The flow evolution is governed by the Boussinesq Navier–Stokes equations, conservation of buoyancy and mass continuity equations. In non-dimensional form, these are

$$\frac{\partial \boldsymbol{u}}{\partial t} + \boldsymbol{u}\cdot\boldsymbol{\nabla}\boldsymbol{u} = -\boldsymbol{\nabla}p + Ri_0 b\hat{\boldsymbol{z}} + \frac{1}{Re_0}\nabla^2\boldsymbol{u}, \tag{2.3}$$

$$\frac{\partial b}{\partial t} + \boldsymbol{u}\cdot\boldsymbol{\nabla}b = \frac{1}{Re_0 Pr}\nabla^2 b, \tag{2.4}$$

$$\boldsymbol{\nabla}\cdot\boldsymbol{u} = 0, \tag{2.5}$$

where $\boldsymbol{u} = \{u,v,w\}$ is the net velocity, b is the buoyancy, p is the pressure and $\hat{\boldsymbol{z}}$ is the vertical unit vector. The equations include three non-dimensional parameters, namely the

https://doi.org/10.1017/jfm.2023.412 Published online by Cambridge University Press

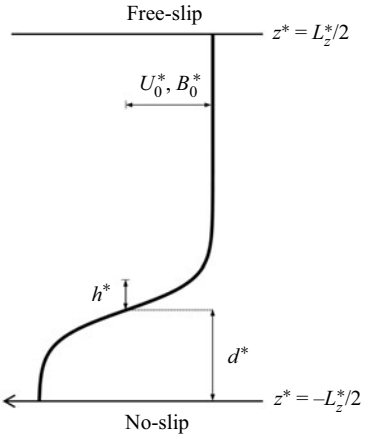

Figure 1. Initial mean profile for buoyancy and velocity showing dimensional parameters and boundary conditions. The bottom boundary moves to the left with speed $-U_0^* \tanh(d^*/h^*)$ for computational efficiency.

initial Reynolds number, $Re_0 = U_0^* h^*/\nu^*$, where ν^* is the kinematic viscosity, the Prandtl number, $Pr = \nu^*/\kappa^*$, where κ^* is the diffusivity, and the initial bulk Richardson number, $Ri_0 = B_0^* h^*/U_0^{*2}$.

In general, the gradient Richardson number is defined by

$$Ri_g = \frac{\partial \langle b^* \rangle_{xy}/\partial z^*}{(\partial \langle u^* \rangle_{xy}/\partial z^*)^2} = Ri_0 \frac{\partial \langle b \rangle_{xy}/\partial z}{(\partial \langle u \rangle_{xy}/\partial z)^2}. \tag{2.6}$$

The notation $\langle\ \rangle_r$ denotes an average over r, where r may represent any combination of x, y, z and t. When $t > 0$, the minimum gradient Richardson number over z is named as Ri_{min}. In the inviscid limit, $Ri_{min} < 1/4$ is a necessary condition for instability (Howard 1961; Miles 1961). For the flow described by (2.2), the initial minimum Ri_g is given by Ri_0.

Boundary conditions are periodic in both horizontal directions. The top boundary is free slip ($\partial u/\partial z = \partial v/\partial z = 0$). The bottom boundary is no slip and moves with velocity $u = -\tanh(d)$, $v = 0$ (figure 1) so that the speed differential between the mean flow and the boundary is ~ 0. The advantage of setting the no-slip boundary as a moving boundary is that the timestep can be larger based on the Courant–Friedrichs–Lewy condition. Both boundaries are insulating ($\partial b/\partial z = 0$) and impermeable ($w = 0$).

A small, random velocity perturbation is added to the initial state (2.2). This initial noise field is purely random and is applied to all three velocity components throughout the computational domain. The maximum amplitude of any one component is 0.05, or 2.5 % of the velocity change across the shear layer, small enough that the initial-growth phase is described by linear perturbation theory. Ensembles of simulations are performed, each using a different seed to generate the random velocities (Liu *et al.* 2022). The choices of d, grid sizes and repetition of runs for each set of simulations are presented in table 1.

2.2. *Linear stability analysis*

To calculate the linear instabilities, (2.3)–(2.5) are linearized about the initial base flow (2.2) and perturbed by small-amplitude, normal mode disturbances proportional to the real part of $a(z)\exp(\sigma t + \mathrm{i}kx)$. Here, $a(z)$ is the vertically varying, complex amplitude of any perturbation quantity, σ is a complex exponential growth rate and k is the wavenumber in the streamwise direction. The phase speed is defined as $c = -\sigma_i/k$, where the subscript

https://doi.org/10.1017/jfm.2023.412 Published online by Cambridge University Press

d	(L_x, L_y, L_z)
10	(28.28, 7.07, 20)
6	(28.56, 7.14, 20)
4	(28.21, 7.05, 20)
3	(28.36, 7.09, 20)
2.5	(27.93, 6.98, 20)
2	(29.16, 7.29, 20)

Table 1. Parameter values for six, 10-member DNS ensembles. In all cases $Re_0 = 1000$, $Pr = 1$, $Ri_0 = 0.12$ and the grid size is $512 \times 128 \times 361$. The maximum initial random velocity component is 0.05.

i denotes the imaginary part. The normal mode equations are expressed in matrix form and discretized using a finite difference method to form a generalized eigenvalue problem (Smyth & Carpenter 2019).

2.3. *Direct numerical simulations*

The simulations are carried out using DIABLO (Taylor 2008), which utilizes a mixed implicit–explicit timestepping scheme with a pressure projection method. The viscous and diffusive terms are handled implicitly with a second-order Crank–Nicolson method; other terms are treated explicitly with a third-order Runge–Kutta–Wray method. The vertical z direction dependence is approximated using a second-order finite difference method, while the periodic streamwise and spanwise (x, y) directions are handled pseudospectrally.

To allow the subharmonic mode to grow, two wavelengths of the fastest-growing KH mode are accommodated in the streamwise periodicity interval L_x based on linear stability analysis (§ 2.2). The spanwise periodicity interval $L_y = L_x/4$ is adequate for the development of 3-D secondary instabilities (e.g. Klaassen & Peltier 1985*b*; Mashayek & Peltier 2013). The domain height is $L_z = 20$, sufficient to avoid boundary effects for simulations of isolated shear layer.

The computational grid is uniform and isotropic. Grid dimensions are chosen to resolve $\sim$2.5 times the Kolmogorov length scale, $L_k = (Re^{-3}/\epsilon')^{1/4}$ after the onset of turbulence.

Due to the sensitive dependence on initial conditions that may greatly alter the evolution of the instability and turbulent mixing (Liu *et al.* 2022), an adequate ensemble size is crucial for controlling sampling error. Therefore, we must compromise between Re, Pr and ensemble size. Since we are focused mainly on the boundary proximity effect, the initial state parameters, Richardson, Reynolds and Prandtl numbers are fixed. We conduct a total of 60 DNS runs, ensembles of 10 cases for different values of d. In all cases, we set $Re_0 = 1000$, the smallest value at which the suppression of pairing is clearly manifested. We choose $Ri_0 = 0.12$, large enough for stratification to be important but small enough for pairing to develop without being entirely damped by stratification. We choose $Pr = 1$, an appropriate value for air but too small to be entirely realistic in water, a compromise that has to be made due to computational resource limits.

2.4. *Diagnostics*

The total velocity field can be decomposed into a horizontally averaged component (the mean flow) and a perturbation (Caulfield & Peltier 2000)

$$\boldsymbol{u}(x, y, z, t) = \bar{U}\hat{\boldsymbol{e}}^{(x)} + \boldsymbol{u}'(x, y, z, t), \quad \text{where } \bar{U}(z, t) = \langle u \rangle_{xy}\,, \tag{2.7}$$

https://doi.org/10.1017/jfm.2023.412 Published online by Cambridge University Press

where $\hat{\boldsymbol{e}}^{(x)}$ is the unit vector in the streamwise direction. The perturbation velocity is further partitioned into 2-D and 3-D components

$$\boldsymbol{u}'(x, y, z, t) = \boldsymbol{u}_{2d} + \boldsymbol{u}_{3d}, \tag{2.8}$$

where

$$\boldsymbol{u}_{2d}(x, z, t) = \langle \boldsymbol{u} \rangle_y - \bar{U}\hat{\boldsymbol{e}}^{(x)} \quad \text{and} \quad \boldsymbol{u}_{3d}(x, y, z, t) = \boldsymbol{u} - \boldsymbol{u}_{2d} - \bar{U}\hat{\boldsymbol{e}}^{(x)} = \boldsymbol{u} - \langle \boldsymbol{u} \rangle_y . \tag{2.9a,b}$$

The buoyancy field can be decomposed in the same manner as the velocity field, therefore the 3-D component can be defined as

$$b_{3d}(x, y, z, t) = b - \langle b \rangle_y. \tag{2.10}$$

Following the decomposition of the velocity, the total kinetic energy can be subdivided as

$$\mathscr{K} = \bar{\mathscr{K}} + \mathscr{K}'; \quad \mathscr{K}' = \langle \mathscr{K}_{2d} \rangle_{xz} + \langle \mathscr{K}_{3d} \rangle_{xyz}, \tag{2.11a,b}$$

where

$$\bar{\mathscr{K}} = \tfrac{1}{2}\left\langle \bar{U}^2 \right\rangle_z, \quad \mathscr{K}_{2d} = \tfrac{1}{2}(u_{2d}^2 + v_{2d}^2 + w_{2d}^2), \quad \mathscr{K}_{3d} = \tfrac{1}{2}\left(u_{3d}^2 + v_{3d}^2 + w_{3d}^2\right). \tag{2.12a–c}$$

These constituent kinetic energies $\bar{\mathscr{K}}$, $\mathscr{K}'$, $\mathscr{K}_{2d}$ and $\mathscr{K}_{3d}$ may be identified, respectively, as the horizontally averaged kinetic energy associated with the mean flow, the turbulent kinetic energy and the kinetic energy associated with 2- and 3-D motions, respectively. The time at which $\langle \mathscr{K}_{3d} \rangle_{xyz}$ is maximum is defined as t_{3d}.

It is also convenient to partition the kinetic energy into components associated with certain wavenumbers by Fourier decomposition. The Fourier transform of the perturbation velocity field at $z = 0$ is

$$\widehat{\boldsymbol{u}'}(k, y, t) = \frac{1}{L_x}\int_0^{L_x} \boldsymbol{u}'(x, y, t)\mathrm{e}^{-\mathrm{i}kx}\,\mathrm{d}x, \tag{2.13}$$

where $k = (2\pi/L_x)n$, $n = 1, 2, 3, \ldots N_x/2 - 1$ and $N_x = 512$ for the array sizes used here. The spectral decomposition of the perturbation kinetic energy is then defined as

$$\widehat{\mathscr{K}'}(k, t) = \tfrac{1}{2}\left(\langle \widehat{u'}\widehat{u'}^* \rangle_y + \langle \widehat{v'}\widehat{v'}^* \rangle_y + \langle \widehat{w'}\widehat{w'}^* \rangle_y\right), \tag{2.14}$$

where $\widehat{u'}^*$ is the complex conjugate of the transformed perturbation velocity component. The turbulent kinetic energy is given by

$$\mathscr{K}'(t) = \sum_{n=1}^{N_x/2-1} \widehat{\mathscr{K}_n'}. \tag{2.15}$$

We denote the subharmonic component as $\mathscr{K}_{sub}$ for $n = 1$, and the KH component as $\mathscr{K}_{KH}$ for $n = 2$. The time at which $\mathscr{K}_{sub}$ and $\mathscr{K}_{KH}$ are maxima are defined as t_{sub} and t_{KH}, respectively.

We calculate the phase spectrum of the perturbation vertical velocity by taking the Fourier transform of $\langle w' \rangle_y$. The result can then be expressed as

$$\widehat{w'}(k, t) = \hat{W}(k)\mathrm{e}^{\mathrm{i}\hat{\phi}(k)}, \tag{2.16}$$

where $\hat{W}(k)$ and $\hat{\phi}(k)$ are, respectively, the amplitude spectrum and the phase spectrum.

https://doi.org/10.1017/jfm.2023.412 Published online by Cambridge University Press

A key process that we wish to quantify is the irreversible mixing. To do so, we decompose the total potential energy $\mathscr{P} = -Ri_0\langle bz\rangle_{xyz}$ into available and background components, $\mathscr{P} = \mathscr{P}_a + \mathscr{P}_b$. Here, $\mathscr{P}_b$ is the minimum potential energy that can be achieved by adiabatically rearranging the buoyancy field into a statically stable state b^* (Winters *et al.* 1995; Tseng & Ferziger 2001). After computing the total and background potential energy, the available potential energy is calculated from the residual, $\mathscr{P}_a = \mathscr{P} - \mathscr{P}_b$; $\mathscr{P}_a$ is the potential energy available for conversion to kinetic energy, which arises due to lateral variations in buoyancy or statically unstable regions.

Following Caulfield & Peltier (2000), we define the irreversible mixing rate due to fluid motions $\mathscr{M}$ as

$$\mathscr{M} = \frac{\mathrm{d}\mathscr{P}_b}{\mathrm{d}t} - \mathscr{D}_p, \tag{2.17}$$

where $\mathscr{D}_p \equiv Ri_0(b_{top} - b_{bottom})/(RePrL_z)$ denotes the rate at which the potential energy of a statically stable density distribution would increase in the absence of any fluid motion (i.e. due only to diffusion of the mean buoyancy profile).

We define the instantaneous mixing efficiency as

$$\eta_i = \frac{\mathscr{M}}{\mathscr{M} + \epsilon}, \tag{2.18}$$

where we use the total dissipation rate $\epsilon = 2/Re\langle s_{ij}s_{ij}\rangle_{xyz}$, and $s_{ij} = (\partial u_i/\partial x_j + \partial u_j/\partial x_i)/2$ is the strain rate tensor. The mixing efficiency relates the fraction of energy that goes into irreversible mixing to the total loss of kinetic energy that is irreversibly lost by the fluid (Peltier & Caulfield 2003). We note that there are a variety of definitions for mixing efficiency in the literature (Gregg *et al.* 2018). A cumulative mixing efficiency is also useful for quantifying the efficiency of the entire mixing event, and is defined as

$$\eta_c = \frac{\displaystyle\int_{t_i}^{t_f} \mathscr{M}\,\mathrm{d}t}{\displaystyle\int_{t_i}^{t_f} \mathscr{M}\,\mathrm{d} + \int_{t_i}^{t_f} \epsilon\,\mathrm{d}t}, \tag{2.19}$$

where $t_i \sim 2.2$ is the initial time after the model adjustment period, and t_f is the final time of the simulation at which $\mathscr{K}'$ drops more than 3 orders of magnitude.

The evolution of kinetic energy equation associated with the 3-D perturbations can be expressed in the form (Caulfield & Peltier 2000)

$$\sigma_{3d} = \frac{1}{2\langle\mathscr{K}_{3d}\rangle_{xyz}}\frac{\mathrm{d}}{\mathrm{d}t}\langle\mathscr{K}_{3d}\rangle_{xyz} \tag{2.20}$$

$$= \mathscr{R}_{3d} + \mathscr{S}h_{3d} + \mathscr{A}_{3d} + \mathscr{H}_{3d} + \mathscr{D}_{3d}, \tag{2.21}$$

where the first two terms represent the 3-D perturbation kinetic energy extraction from the background mean shear and the background 2-D KH billow by means of Reynolds stresses, respectively defined as

$$\mathscr{R}_{3d} = -\frac{1}{2\langle\mathscr{K}_{3d}\rangle_{xyz}}\left\langle u_{3d}w_{3d}\frac{\partial\bar{U}}{\partial z}\right\rangle_{xyz}, \tag{2.22}$$

$$\mathscr{S}h_{3d} = -\frac{1}{2\langle\mathscr{K}_{3d}\rangle_{xyz}}\left\langle (u_{3d}w_{3d})\left(\frac{\partial u_{2d}}{\partial z} + \frac{\partial w_{2d}}{\partial x}\right)\right\rangle_{xyz}. \tag{2.23}$$

https://doi.org/10.1017/jfm.2023.412 Published online by Cambridge University Press

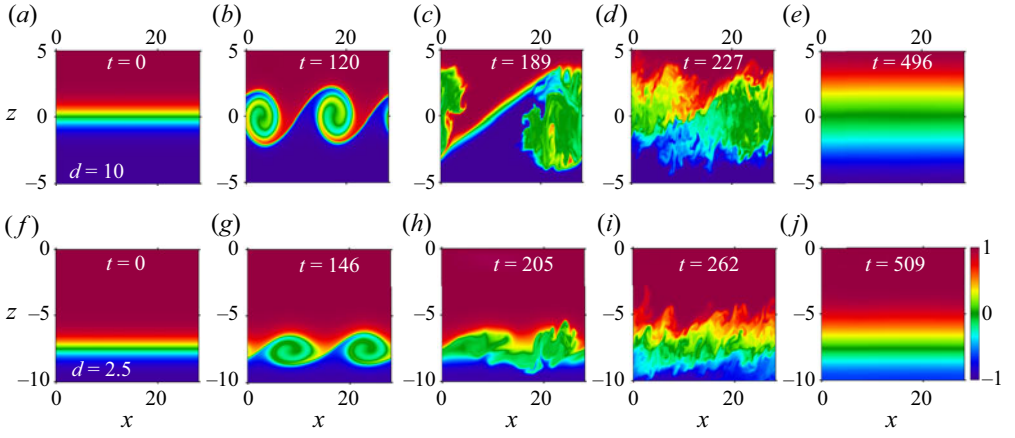

Figure 2. Cross-sections through $y = 0$ at various times for (*a–e*) shear layer far from boundary ($d = 10$, case #3), (*f–j*) shear layer close to boundary ($d = 2.5$, case #1). Panels (*b*,*g*) are at their respective t_{KH}.

The third term represents the stretching/compression of the 3-D vorticity and is defined as

$$\mathscr{A}_{3d} = -\frac{1}{2\langle \mathscr{K}_{3d}\rangle_{xyz}}\left\langle \frac{1}{2}\left(u_{3d}^2 - w_{3d}^2\right)\left(\frac{\partial u_{2d}}{\partial x} - \frac{\partial w_{2d}}{\partial z}\right)\right\rangle_{xyz}. \tag{2.24}$$

The final two terms are the buoyancy production term and the negative–definite viscous dissipation term associated with 3-D perturbations and are defined, respectively, as

$$\mathscr{H}_{3d} = \frac{Ri_0}{2\langle \mathscr{K}_{3d}\rangle_{xyz}}\langle b_{3d}w_{3d}\rangle_{xyz}, \tag{2.25}$$

$$\mathscr{D}_{3d} = -\frac{1}{\langle \mathscr{K}_{3d}\rangle_{xyz}Re}\langle s_{ij}s_{ij}\rangle_{xyz}, \tag{2.26}$$

where s_{ij} is the strain rate tensor of the 3-D motions. There are no additional terms in (2.21) associated with boundary fluxes, but all terms are ultimately affected by the boundary.

3. Overview

Consider a tanh shear layer (as in figure 1) with $Ri_{min} < 1/4$ and weak viscosity and diffusion located far from any boundary (figure 2*a*). The incipient KH instability grows to macroscopic amplitude and generates a train of KH billows of which our computational domain contains two (figure 2*b*). In the next phase, adjacent billows pair (figure 2*c*). Thereafter, the billow structure breaks down as 3-D secondary instabilities create turbulence (figure 2*d*). Finally, the flow relaminarizes. The shear layer is now stable because $Ri_{min} > 1/4$ (figure 2*e*).

When the instability occurs near the boundary ($d = 2.5$; figure 2*f–j*), the evolution of the KH instability has some resemblance to the $d = 10$ cases. The linear instability grows to finite amplitude (figure 2*g*), then 3-D secondary instabilities arise and turbulence is generated, breaking down the KH billows (figure 2*h*,*i*). Finally, the flow relaminarizes to a stable state (figure 2*j*). When $d = 2.5$, the vertical extent of the KH billow at $t = t_{KH}$ (figure 2*g*) is 55 % of that for $d = 10$ (figure 2*b*). In other words, KH billows are flatter when the shear layer is closer to the boundary. (The vertical extent of the billows is defined

https://doi.org/10.1017/jfm.2023.412 Published online by Cambridge University Press

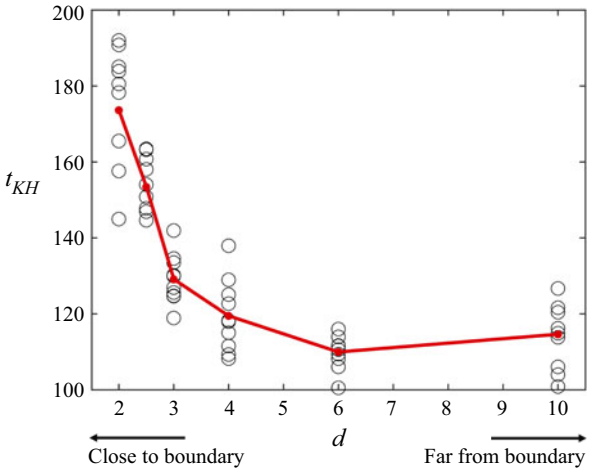

Figure 3. Dependence of t_{KH} on d. Circles denote all ensemble members. Red represents the mean.

as the distance between two local maximum buoyancy gradients at the upper and lower edges of the billows.) This result is consistent with previous laboratory experiments (Holt 1998). The geometrical change occurs because the impermeable boundary constrains the vertical development of the billows.

Another impact of the boundary is that the primary KH instability grows slower so the onset of turbulence is delayed. The maximum $\mathscr{K}_{KH}$ occurs at $t_{KH} = 120$ for $d = 10$ (figure 2*b*) but is delayed to $t_{KH} = 145$ for $d = 2.5$ (figure 2*g*). A more robust demonstration of the boundary effect on the KH evolution is the dependence of t_{KH} on d (figure 3). When the boundary effect becomes salient, e.g. $d < 4$, t_{KH} increases significantly with decreasing d.

4. Pairing

In a train of KH billows, there is a range of different wavelengths including the primary KH wavelength, along with its shorter harmonics and longer subharmonics. Like all interfacial disturbances, KH instability decays exponentially and vertically away from the interface (Smyth & Carpenter 2019). The decay depth is proportional to the wavelength. Therefore, we can expect that the subharmonic mode (twice the wavelength of the fastest-growing KH mode) is influenced by the boundary most strongly because it has the greatest vertical reach. In this section, we explore the mechanisms whereby the subharmonic instability is affected by the boundary.

4.1. *Energy evolution*

The evolution of $\mathscr{K}_{KH}$ and $\mathscr{K}_{sub}$ with different values of d is shown in figure 4. The dependence of these energies on d can be viewed as two distinct regimes. The change of $\mathscr{K}_{KH}$ and $\mathscr{K}_{sub}$ is slight when $d \geqslant 4$ (red, blue and green curves are close together), but precipitous when $d < 4$ (orange, purple and yellow curves are widely separated). We interpret this to mean that boundary effects become significant when $d < 4$.

One possible consequence of subharmonic instability is pairing, which can increase mixing significantly (Rahmani *et al.* 2014). However, pairing is found mainly in idealized simulations and laboratory experiments; it is rarely observed in geophysical flows.

https://doi.org/10.1017/jfm.2023.412 Published online by Cambridge University Press

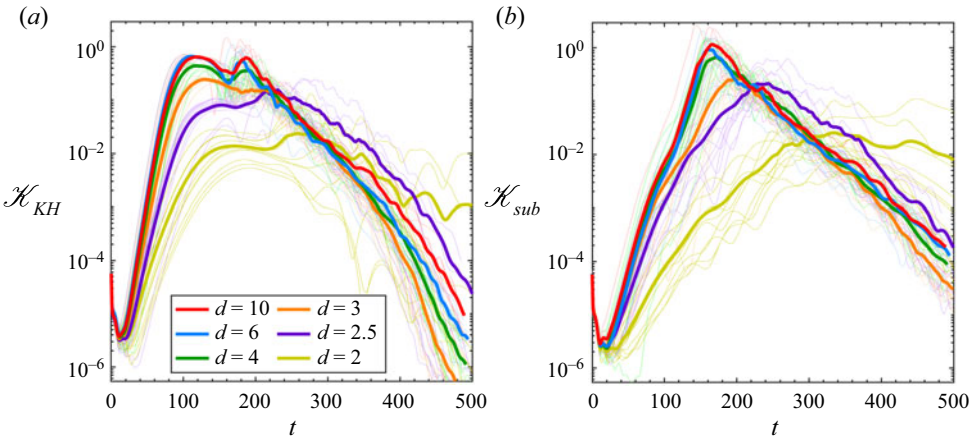

Figure 4. Time variation of kinetic energy of the (*a*) primary KH and (*b*) subharmonic Fourier components with different values of d. Each thick curve represents the average of all cases with the same d.

A possible explanation is provided by the discovery that, at high Reynolds number, pairing can be suppressed by the early emergence of a 'zoo' of 3-D secondary instabilities (Mashayek & Peltier 2011, 2013, 2012*b*). Another well-known mechanism that suppresses pairing is background stratification, which restricts vertical motion, thereby stabilizing the subharmonic mode whenever Ri_0 exceeds approximately 3/16 (i.e. instability requires $Ri_0 < k(1-k)$ and the subharmonic wavenumber is $k \simeq 1/4$, e.g. Smyth & Carpenter 2019, § 4.4). In the present simulations, we ensure that pairing is not prevented by either 3-D secondary instability or stratification by choosing $Re_0 = 1000$ and $Ri_0 = 0.12$ for all cases.

Here, we propose that the boundary can be another important factor in suppressing pairing. In the examples shown in figure 2, pairing occurs when $d = 10$ but not when $d = 2.5$. To generalize the distinction, we examine the ensemble average of many cases (figure 4*b* and 5) over a range of d values. Similar to the dependence on Re (Mashayek & Peltier 2013, figure 21), we find that the maximum of $\mathscr{K}_{sub}$ decreases monotonically with decreasing d. Therefore, the boundary effect has similar influence on pairing to the Reynolds number effect, although the underlying mechanism is different.

The spread of $\mathscr{K}_{sub}^{max}$ tends to be larger when d is large (figure 5). This is because the pairing process is sensitive to small changes in the initial conditions. Billow evolution can be categorized as laminar pairing, turbulent pairing or non-pairing (Dong *et al.* 2019; Guha & Rahmani 2019; Liu *et al.* 2022). Laminar pairing involves the greatest amount of subharmonic kinetic energy (blue circles in figure 5), because at the time when $\mathscr{K}_{sub}$ is a maximum, turbulence has not yet grown strong enough to collapse the coherent billow structure. When the boundary effect is negligible (e.g. when $d = 10$), laminar pairing occurs in a single case. Other cases with $d = 10$ produce turbulent pairing (green circles), in which turbulence drains part of the kinetic energy from the emerging paired billow. When the shear layer is located close to the boundary, the maximum subharmonic kinetic energy decreases. Furthermore, more cases fail to pair (red circles). Among cases that successfully pair, most are already turbulent (turbulent pairing, green circles), while laminar pairing becomes less likely. The spread of $\mathscr{K}_{sub}^{max}$ between cases is usually smaller when d is small.

One might expect that the suppression of pairing by the boundary would be accomplished via damping of the subharmonic KH instability, and such damping is in fact

https://doi.org/10.1017/jfm.2023.412 Published online by Cambridge University Press

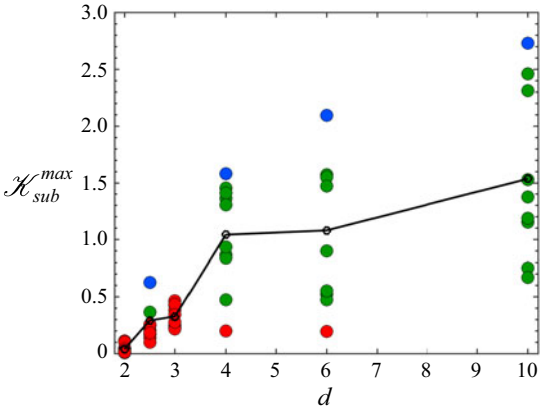

Figure 5. Dependence of maximum subharmonic kinetic energy on d. The ensemble members exhibiting laminar pairing, turbulent pairing and non-pairing are represented by blue, green and red circles, respectively, while the mean is indicated by the black line.

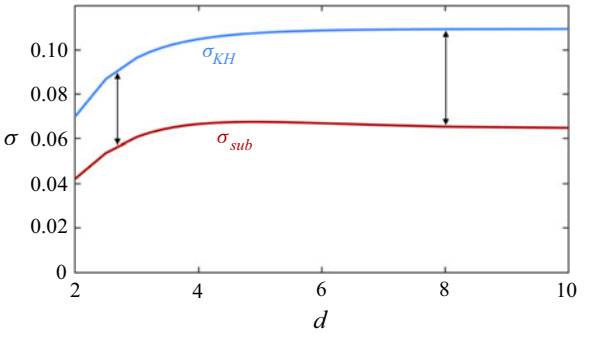

Figure 6. Dependence of KH growth rate and subharmonic growth rate on d from linear stability analysis with $Ri_0 = 0.12$, $Re_0 = 1000$ and $Pr = 1$.

found for $d < 4$ (figure 6, red curve). However, a hint that the mechanism is more subtle than this is revealed by the growth rate of the primary KH mode, σ_{KH} (figure 6, blue curve), which decreases even more than does σ_{sub}, i.e. the growth rate of the subharmonic relative to the primary increases. Based only on this comparison of growth rates, one would expect pairing to take longer but to actually be more pronounced at low d, contrary to figure 2. We will describe the mechanism whereby the boundary effect suppresses pairing in the following subsection.

4.2. *Phase evolution*

The optimal separation between the KH and subharmonic modes is

$$\Delta_{sub}^{KH} \equiv \frac{x_{KH} - x_{sub}}{\lambda_{KH}} = \frac{3}{4} + n, \tag{4.1}$$

where n is an arbitrary integer, λ_{KH} is the wavelength of the KH mode and x_{KH} and x_{sub} are the crest positions of the KH and subharmonic vertical velocity profiles, respectively (figure 7*a*). These positions are computed from the Fourier phase spectrum of the centreline vertical velocity. In this configuration, one KH billow is lifted and its neighbour

https://doi.org/10.1017/jfm.2023.412 Published online by Cambridge University Press

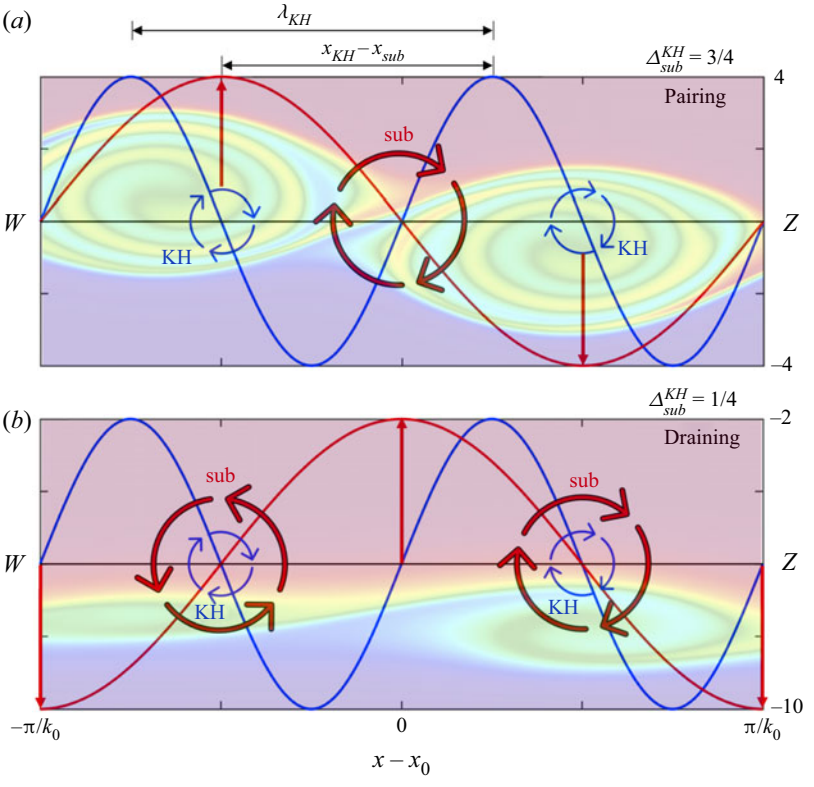

Figure 7. Schematic of vorticity and vertical motions in terms of the subharmonic and KH modes at the onset of (*a*) pairing instability with optimal $\Delta_{sub}^{KH}=3/4$ ($d=10$, case #7) and (*b*) draining instability with optimal $\Delta_{sub}^{KH}=1/4$ ($d=2.5$, case #2). Buoyancy snapshots in the background of both panels demonstrate the corresponding structure. Here, k_0 is the subharmonic wavenumber and x_0 is a midway point between billows.

is lowered by the vertical motion of the subharmonic mode (figure 7*a*). Thereafter, the mean shear feeds energy to the pairing billows, and a single vortex is formed (Dong *et al.* 2019; Guha & Rahmani 2019). The opposite value of the optimal Δ_{sub}^{KH} is $1/4+n$ (figure 7*b*). In this case, one vortex rotates in the same direction as the subharmonic vorticity, while the other one rotates oppositely and is thus cancelled out. This process is referred to as draining (Klaassen & Peltier 1989).

The evolution of Δ_{sub}^{KH} (figure 8) shows that the KH and subharmonic modes require some time to lock on. The onset and end of the lock-on process are ambiguous, especially when d is small. Nonetheless, the lock-on period can be qualitatively viewed as the period during which the change of Δ_{sub}^{KH} is the smallest (i.e. the dotted curve is most nearly horizontal). For $d=10$ (figure 8*a*), the lock-on value is $3/4$ from approximately $t\sim 100$ to 150 during which time pairing occurs. The highlighted red coloured case locks on to the pairing position $\Delta_{sub}^{KH}=3/4$ relatively early, $t\sim 100$. The corresponding buoyancy field is shown in the background of figure 7(*a*), in which laminar pairing can be seen. In the paired state (e.g. $t=170$), when billows are replaced by a single vortex, Δ_{sub}^{KH} switches to $1/4$. After the flow becomes turbulent, Δ_{sub}^{KH} fluctuates chaotically because the billows break down into turbulence, therefore Δ_{sub}^{KH} is not meaningful.

In cases with lower d, several changes complicate the lock-on process: (i) Δ_{sub}^{KH} changes in time more rapidly, (ii) the time during which phase locking is sustained decreases

https://doi.org/10.1017/jfm.2023.412 Published online by Cambridge University Press

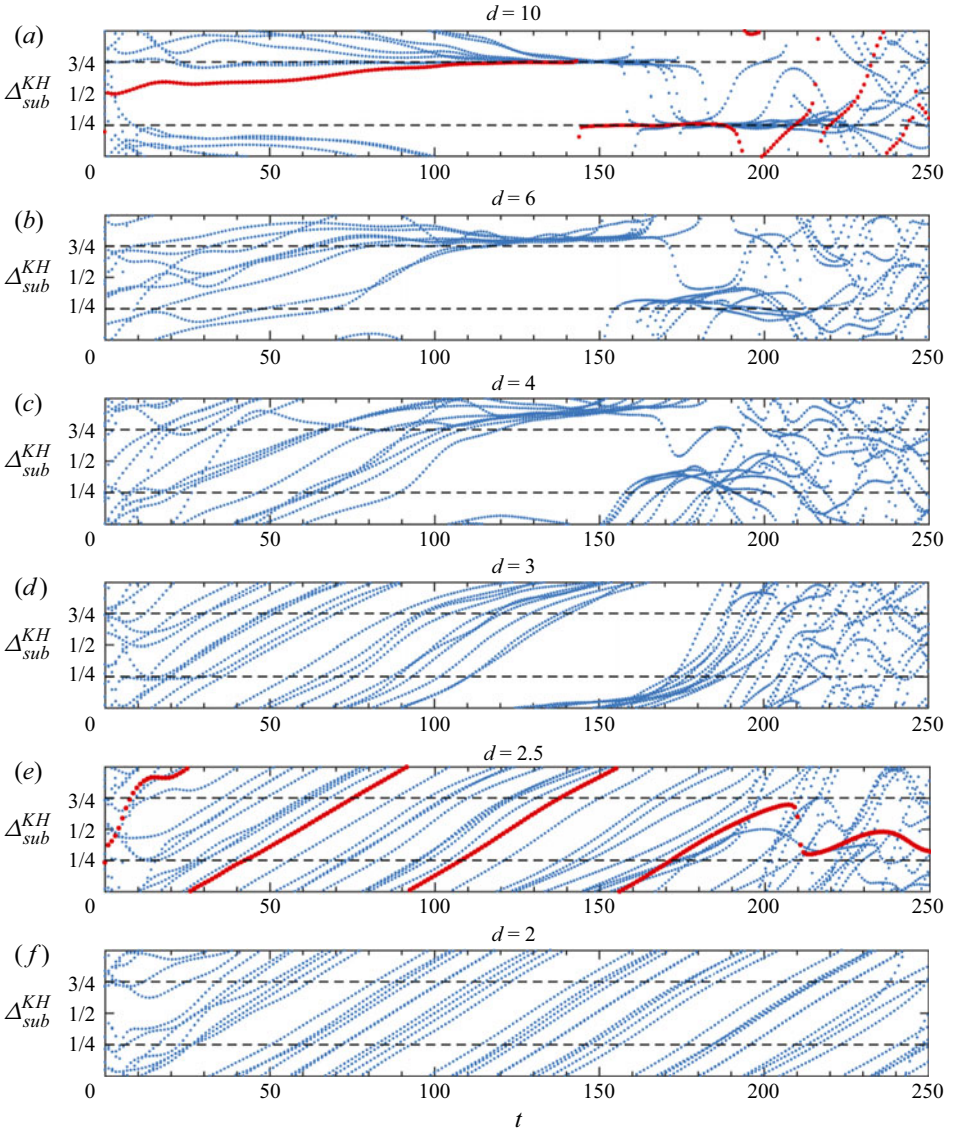

Figure 8. Time variations of Δ_{sub}^{KH} with different values of d. Two horizontal dashed lines in each panel denote the optimal lock-on value, $\Delta_{sub}^{KH} = 3/4$, and the opposite of optimal value, $\Delta_{sub}^{KH} = 1/4$, respectively. Red curves indicate the cases selected in figure 7.

and (iii) the value of Δ_{sub}^{KH} at which phase locking occurs departs from 3/4, eventually approaching 1/4 (figure 8*b–e*). For $d = 6$, the lock-on value is slightly larger than 3/4 during $t \sim 110$ to 150 (figure 8*b*); for $d = 4$, the lock-on value is $\sim 7/8$ during $t \sim 120$–150 (figure 8*c*) and, for $d = 3$, the lock-on value increases to ~ 1 or equivalently 0 (i.e. x_{KH} and x_{sub} at the same position) during $t \sim 150$ to 170 (figure 8*d*). When $d = 2.5$ (figure 8*e*), the lock-on value becomes less clear because the time variation of Δ_{sub}^{KH} increases. Nonetheless, we can still roughly estimate the lock-on value by determining the time at which most cases converge to a similar Δ_{sub}^{KH} value. With this approach, a reasonable lock-on value is 1/4 at $t \sim 170$ (figure 8*e*), which coincides with the optimal

https://doi.org/10.1017/jfm.2023.412 Published online by Cambridge University Press

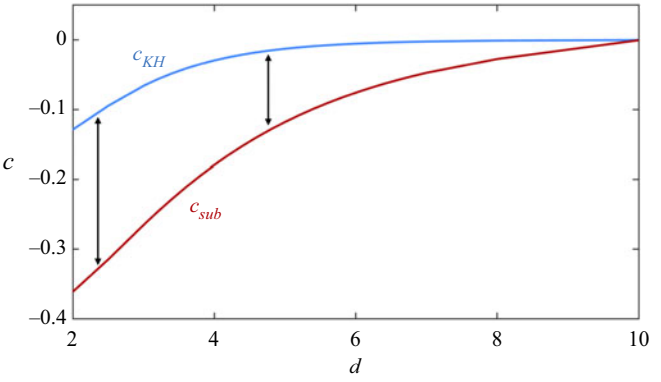

Figure 9. Dependence of KH phase speed and subharmonic phase speed on d from linear stability analysis with $Ri_0 = 0.12$, $Re = 1000$ and $Pr = 1$.

value for draining. The buoyancy field of the red-highlighted case, in which one vortex is enhanced while the other is suppressed, is shown in the background of figure 7(*b*). This result does not imply that draining always occurs when $d = 2.5$; draining can often be absent depending on the details of the initial conditions (Liu *et al.* 2022).

It is not a coincidence that the draining lock-on value for the case $d = 2.5$ and the paired state lock-on value for the case $d = 10$ (e.g. $t = 150$) are both $\Delta_{sub}^{KH} \simeq 1/4$. This is because the pairing and draining mechanisms, though very different, both transform a pair of billows into a single vortex. When d is even smaller ($d = 2$), the lock-on value and period are highly ambiguous. The boundary effect prevents the KH and subharmonic phases from locking on altogether, and therefore pairing is suppressed.

The phase difference Δ_{sub}^{KH} at $t = 0$ exhibits substantial variability in all cases; however, this variability diminishes considerably during phase locking. This indicates that the phase-locking value is not significantly contingent upon the initial random noise. When the boundary effect is prominent, significant variability is evident between simulations from the beginning to the end.

For the small-d cases (figure 8*e*,*f*), the steady, rapid increase of Δ_{sub}^{KH} suggests an ongoing change in the phase speeds of the KH and subharmonic modes. This is confirmed by linear stability analysis (figure 9). The fastest-growing KH instability has a phase speed c_{KH} while its subharmonic has half the KH wavenumber by definition, and the phase speed is c_{sub}. When the boundary effects are negligible ($d = 10$), both c_{KH} and c_{sub} are $\sim$0. However, when the shear layer is closer to the boundary, the phase speeds diverge. Therefore, x_{KH} and x_{sub} are constantly changing, which explains the constant change of Δ_{sub}^{KH} seen in figure 8(*b–f*). Thus, boundary proximity impedes phase locking of the KH and subharmonic modes by causing their phase speeds to diverge. In extreme cases of small d (figure 8*f*), phase locking and pairing are prevented altogether.

The dependence of the phase speed difference between the KH and subharmonic modes on the parameters Re_0, Pr and Ri_0 is also of interest as a step toward a broader exploration of the parameter space. The KH instabilities change very little with increasing Re_0 once Re_0 exceeds $\sim O(10^2)$ (Smyth *et al.* 2013); hence, we see little dependence of the phase speed difference $c_{KH} - c_{sub}$ (figure 10*a*). The same is true of the Prandtl number (figure 10*b*). There is a slight dependence on Ri_0 (figure 10*c*) when d is small: the contour (thick contour) corresponding to the phase speed difference found at $Ri_0 = 0.12$, $d = 4$ varies between $d = 3.7$ at very low Ri_0 and $d = 4.6$ at high Ri_0. Therefore the threshold $d \sim 4$ for the suppression of phase locking (and thus pairing) by boundary effects may

https://doi.org/10.1017/jfm.2023.412 Published online by Cambridge University Press

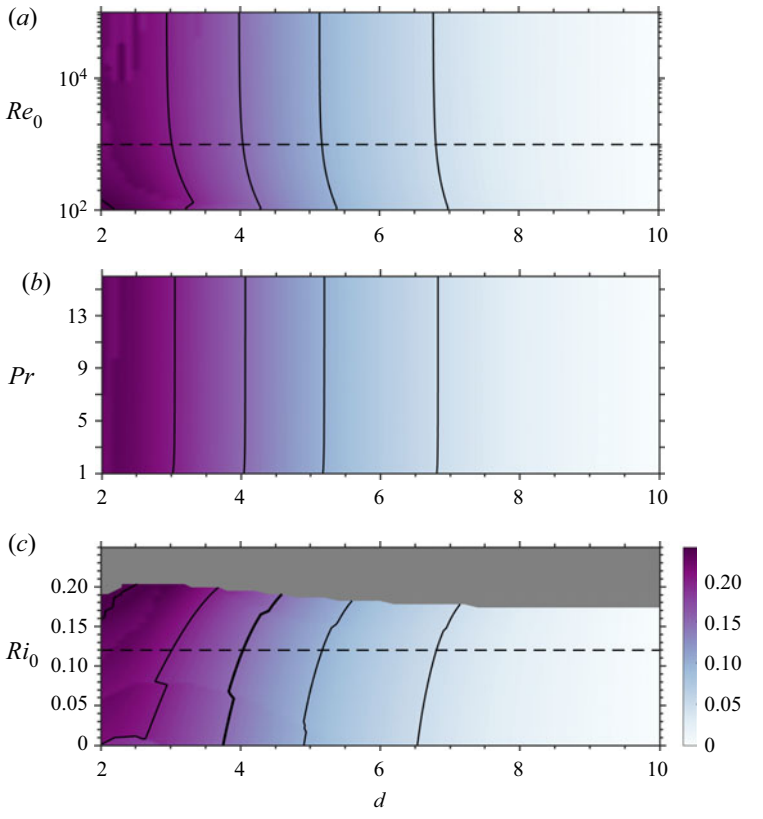

Figure 10. Phase speed difference between unstable KH and subharmonic modes. A non-zero phase speed difference indicates that the KH and subharmonic modes phase lock only if forced to do so by nonlinear effects. (*a*) Relationship between d and Re_0 at a fixed value of $Ri_0 = 0.12$ and $Pr = 1$. (*b*) Relationship between d and Pr at a fixed value of $Ri_0 = 0.12$ and $Re_0 = 1000$. (*c*) Relationship between d and Ri_0 at $Re_0 = 1000$ and $Pr = 1$. The growth rate in the shaded region of (*c*) is below the cutoff value, 0.001. Black contours represent phase speed difference with an interval of 0.05. Horizontal dashed lines indicate $Re_0 = 1000$ and $Ri_0 = 0.12$, respectively, in (*a*,*c*).

vary only weakly with Ri_0. Further DNS is needed to explore the dependence of boundary effects on these parameters in the nonlinear regime.

5. Three-dimensional secondary instabilities

Three-dimensional secondary instabilities catalyze the transition to turbulence, which in turn leads to irreversible mixing. Various 3-D secondary instabilities have been discovered; notably, the shear-aligned convective instability (Davis & Peltier 1979; Klaassen & Peltier 1985*b*) appears when KH billows become large enough to overturn the buoyancy gradient. Herein, we focus on some of the instabilities that help to explain the sources and sinks of 3-D perturbation kinetic energy in shear layers centred at different distances from the boundary. We begin by examining the case $d = 10$, where boundary effects are negligible (§ 5.1). We then examine differences that arise when $d = 2.5$ (§ 5.2) and boundary effects are dominant.

https://doi.org/10.1017/jfm.2023.412 Published online by Cambridge University Press

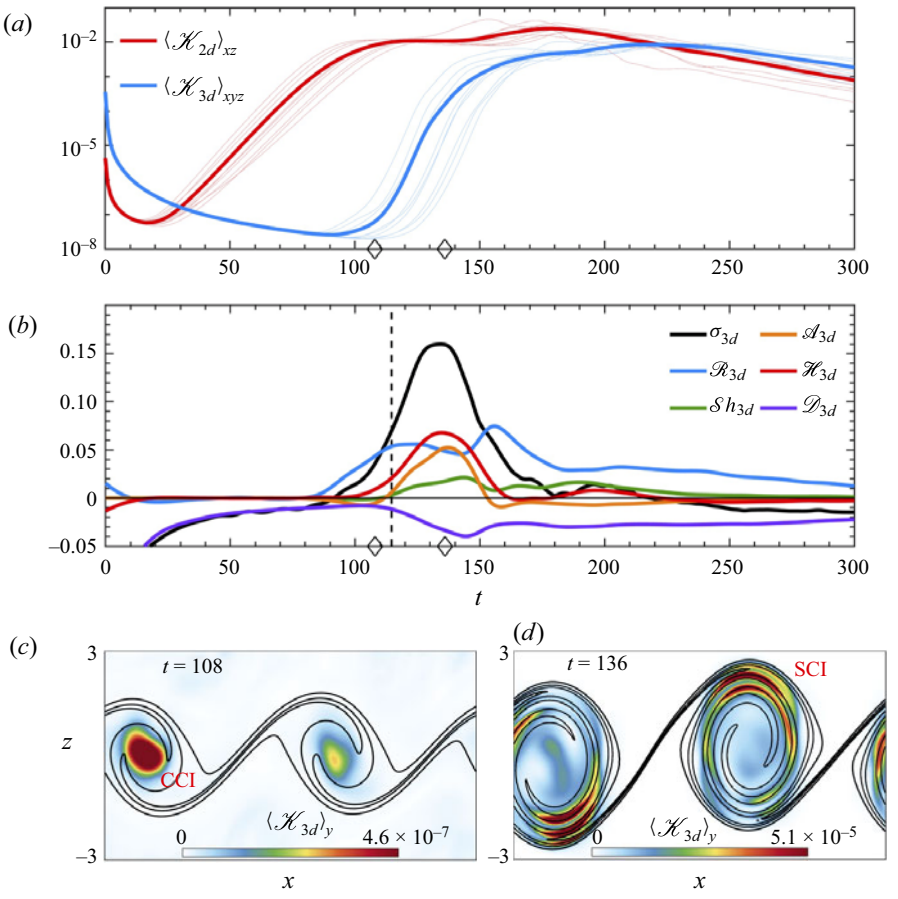

Figure 11. Negligible boundary effect when $d = 10$. (*a*) Time variation of 2-D and 3-D volume-averaged kinetic energy. The thick line is ensemble averaged and thin lines represent all cases. (*b*) Time variation of different terms of the σ_{3d} evolution equation (2.21). All terms are ensemble averaged. Vertical dashed lines represent ensemble-averaged t_{KH}. For clarity in plotting, lower resolution time series have been interpolated to higher temporal resolution using cubic splines. (*c*,*d*) Show spanwise-averaged $\mathscr{K}_{3d}$ for $d = 10$, case #3 at $t = 108$ and $t = 136$, respectively. The contour lines represent spanwise-averaged buoyancy with an interval of 0.4. Note that the colour scales for (*c*,*d*) are different. Times correspond to the diamond symbols in (*a*,*b*).

5.1. *The case $d = 10$: negligible boundary effects*

Three-dimensional secondary instabilities grow mostly between $t \sim 90$ and $t \sim 180$ (figure 11*a*, blue curve). This growth starts after the saturation of the primary KH instability, when $\langle \mathscr{K}_{2d} \rangle_{xz}$ starts to decline (red curve). Two times, indicated by the diamonds in figure 11(*a*), have been selected to illustrate the form of the 3-D motions in terms of the spanwise-averaged $\mathscr{K}_{3d}$. The first of these represents the early growth of $\langle \mathscr{K}_{3d} \rangle_y$ ($t = 108$, figure 11*c*), the second the time of most rapid growth ($t = 136$).

The form of the 3-D motions changes because the KH billow develops different 3-D instabilities as its geometry evolves. We therefore focus on the 3-D perturbation kinetic energy evolution to explain the changes. In the early stage ($0 < t < 90$), there is no 3-D instability. Growth is negative due mostly to viscous dissipation of the initial noise field.

During the earliest stage of 3-D growth, represented by time $t = 108$ (first diamond in figure 11*b*), 3-D motions are concentrated in the cores of the KH billows (figure 11*c*)

https://doi.org/10.1017/jfm.2023.412 Published online by Cambridge University Press

and the $\mathscr{K}_{3d}$ budget is dominated by the shear production term $\mathscr{R}_{3d}$ (figure 11*b*). This is because the spanwise vortex tube at the core of each billow is distorted sinusoidally. Spanwise vorticity is thus redirected towards the x–z plane such that the Reynolds stress $\langle u_{3d}w_{3d}\rangle_{xyz}$ becomes negative (as illustrated in Smyth 2006, figure 8). This 3-D stress field works with the mean shear $\mathrm{d}\bar{U}/\mathrm{d}z$ to produce 3-D kinetic energy. Since $\mathrm{d}\bar{U}/\mathrm{d}z$ is large near the billow core, the shear production quantified by $\mathscr{R}_{3d}$ is dominant. This 3-D secondary instability exhibits similar characteristics to the central-core mode found in Klaassen & Peltier (1991), hence we identify it as central-core instability (CCI).

During the maximum growth stage ($t = 136$, second diamond in figure 11*b*), 3-D motions in the central core are no longer dominant as $\langle\mathscr{K}_{3d}\rangle_y$ is mainly concentrated at the margins of the billows (figure 11*d*). At this stage, the primary KH billows roll up. This results in regions of statically unstable buoyancy variation within and surrounding the billow cores. The buoyancy production $\mathscr{H}_{3d}$ becomes the dominant energy source while $\mathscr{A}_{3d}$ and $\mathscr{S}h_{3d}$ also increase. This is all consistent with the emergence of shear-aligned convection rolls via the secondary convective instability (SCI; Klaassen & Peltier 1985*a*). Vorticity is created when vortex tubes are stretched and is exchanged between different components when vortex tubes bend and tilt. The 2-D velocity gradients increase along with the stretching and bending of vortex tubes surrounding the billows, the stretching deformation term, $\mathscr{A}_{3d}$, and the shear deformation term, $\mathscr{S}h_{3d}$, both increase.

Beyond the time when σ_{3d} is a maximum, the billows start to pair at $t \sim 150$, and $\mathscr{R}_{3d}$ regains its dominance over the other terms. The shear-aligned convection rolls are still active at the periphery of the billow core, but gradually break down into turbulence; therefore $\mathscr{H}_{3d}$ declines toward zero. After the pairs of billows have amalgamated, the extraction of 3-D perturbation kinetic energy from the background mean shear decreases. During the post-turbulent stage, all terms gradually decay.

The fact that the evolution of $\mathscr{R}_{3d}$ when boundary effects are negligible includes two local maxima is consistent with the findings of Mashayek & Peltier (2013). However, they found that, prior to billow saturation, buoyancy production is the major source term while we found that $\mathscr{R}_{3d}$ is dominant. The difference may be due to a difference in the initial random noise field – Mashayek & Peltier (2013) applied noise to both the buoyancy and velocity fields whereas we perturbed only the velocity.

5.2. *The case $d = 2.5$: strong boundary effects*

When the boundary effect is strong (e.g. $d = 2.5$), growth rates of both $\langle\mathscr{K}_{2d}\rangle_{xz}$ and $\langle\mathscr{K}_{3d}\rangle_{xyz}$ are reduced relative to cases with negligible boundary effects (compare figures 11*a* and 12*a*), as are their maximum values.

At maximum growth ($t = 176$, figure 12*d*), there are neither clear unstable sublayers nor 3-D motions in layers surrounding the billows. Instead, $\langle\mathscr{K}_{3d}\rangle_y$ remains concentrated in the core, suggesting that SCI is suppressed. A conspicuous impact of the boundary is that $\mathscr{R}_{3d}$ dominates all other source terms from the initial-growth stage of the instability to the post-turbulent stage (figure 12*b*), rather than being supplanted by $\mathscr{H}_{3d}$ as the primary billows roll up (cf. § 5.1). The terms $\mathscr{H}_{3d}$ (red line in figure 12*b*), $\mathscr{A}_{3d}$ and $\mathscr{S}h_{3d}$ are small throughout the evolution because the overturning within the billow is suppressed by the boundary. This suggests that the balance is mostly between the energy extraction from the background mean shear and the viscous dissipation of the 3-D perturbations.

We conclude that three-dimensionalization is via CCI alone when the boundary effect is strong (figure 12*c*,*d*).

https://doi.org/10.1017/jfm.2023.412 Published online by Cambridge University Press

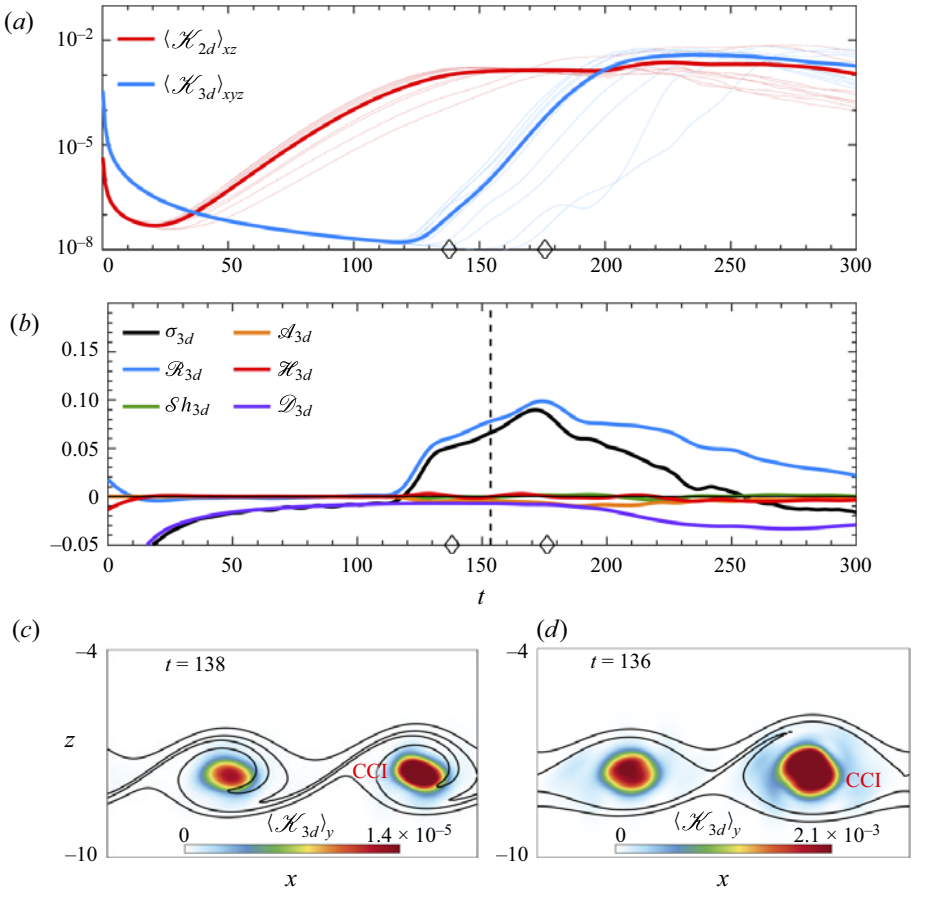

Figure 12. Similar to figure 11 but with the case $d = 2.5$. Case #1 is selected for (*c*,*d*).

5.3. *Effects of boundary proximity on SCI*

We have seen that, for the single case $d = 2.5$, the main effect of the boundary on 3-D instabilities is the suppression of SCI. The Rayleigh number provides a compact metric for SCI that we can examine as a function of d, thus gaining a more comprehensive view of the boundary proximity effect. We define the Rayleigh number at t_{KH} for the statically unstable regions (Klaassen & Peltier 1985*b*) as

$$Ra = -Re^2 Ri_0 Pr \frac{\partial \bar{b}}{\partial z} \delta^4, \tag{5.1}$$

where $\partial \bar{b}/\partial z$ is the average buoyancy gradient across the most unstable layer, and δ is its dimensionless thickness. The critical Ra for convective instability in a layer with free-slip upper and lower boundaries, an approximation to the superadiabatic regions found here, is $Ra_c \approx 657.5$ (e.g. Smyth & Carpenter 2019).

When $d \geqslant 4$ (figure 13), Ra is more than 1 order of magnitude larger than Ra_c, suggesting that SCI is prominent. A precipitous drop in Ra can be seen when $d < 4$, indicating that the boundary suppresses SCI (as seen in figure 12).

Most cases for $d = 2$ fail to satisfy the criterion $Ra > Ra_c$, and as a result, convective motions are suppressed within the KH billow.

https://doi.org/10.1017/jfm.2023.412 Published online by Cambridge University Press

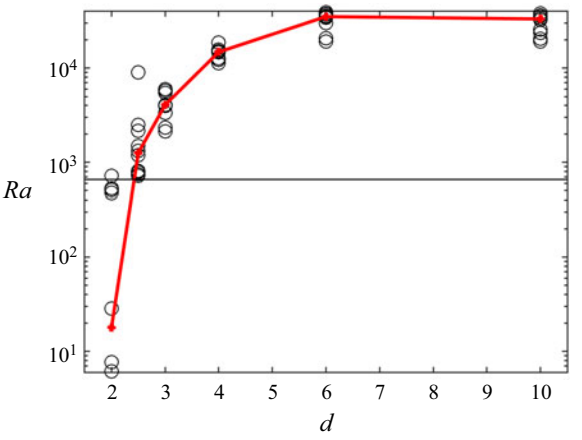

Figure 13. Dependence of Rayleigh number on d at t_{KH}. Circle symbols are all ensemble cases and red dots indicate the mean of the ensembles. Horizontal line denotes the critical Rayleigh number Ra_c, and has a value of 657.5.

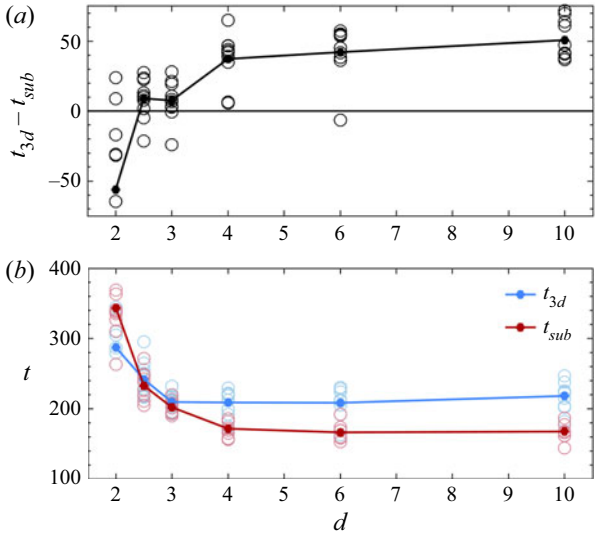

Figure 14. (*a*) Dependence of time difference between t_{3d} and t_{sub} on d. (*b*) Dependence of t_{3d} and t_{sub} on d. Circles are all ensemble cases. Data points represent the ensemble mean. The deviated cases of $d = 2$ are not shown in the figure.

5.4. *Timing of subharmonic and 3-D secondary instabilities*

The timing of the turbulence emergence relative to the subharmonic instability is critical to pairing (Mashayek & Peltier 2013; Liu *et al.* 2022) and therefore to mixing. Thus, t_{sub} and t_{3d} are useful measures for understanding the competition between the subharmonic and 3-D secondary instabilities. The difference between t_{3d} and t_{sub} tends to decrease as d decreases (figure 14*a*). This suggests that the subharmonic instability is more susceptible to interference by turbulence when the boundary effect is strong. (The slope of the mean $t_{3d} - t_{sub}$ vs d is reversed between $d = 2.5$ and $d = 3$, but the reversal is not statistically significant.)

https://doi.org/10.1017/jfm.2023.412 Published online by Cambridge University Press

To identify the source of this behaviour, we next focus on t_{sub} and t_{3d} individually (figure 14*b*). A monotonic increase of t_{sub} with decreasing d can be seen (figure 14*b*); the increase becomes more pronounced when $d < 4$. Thus, $\mathscr{K}_{sub}$ requires more time to reach to its maximum when the boundary effect is greater. The increase of t_{sub} is owing to the fact that phase lock between the KH and subharmonic modes is prevented due to the divergence of the corresponding phase speeds (§ 4).

The increase of t_{3d} with decreasing d when $d < 4$ is due to suppression of 3-D secondary instabilities by the boundary, as has been demonstrated in § 5.2. Even though t_{sub} increases considerably at $d = 2$ and $d = 2.5$, 3-D secondary instabilities (and hence the onset of turbulence) are also delayed. Therefore, subharmonic instability may arise at $d = 2.5$ because turbulence emerges too late to overtake it. When $d = 2$, the subharmonic does not reach maximum amplitude until after 3-D secondary instabilities have already appeared.

6. Turbulent mixing

In the latter part of each simulation, the flow consists of slowly decaying sheared turbulence. The energy in the 3-D motions is supported mainly by shear production (figures 11*b* and 12*b*, blue curves) and diminished by viscosity (purple curves). We now discuss the energy budget of this turbulence in the context of irreversible mixing. The instantaneous mixing efficiency has been calculated using (2.18) and is shown in figure 15(*c*), as are the irreversible mixing rate (figure 15*a*) and the total dissipation rate (figure 15*b*) for various boundary proximity values. Initially, a large dissipation rate arises due mainly to the viscous decay of the random noise. Dissipation rapidly decreases to a near-constant (although non-zero) value as the mean flow continues to diffuse (figure 15*b*), while the mixing rate is near zero.

For all d, the instantaneous mixing rate $\mathscr{M}$ and mixing efficiency exhibit two peaks (figure 15*a*,*c*). The first peak of $\mathscr{M}$ and η_i (e.g. at $t \sim 130$, $d = 10$) is associated with the roll up of the KH billows. Because they are not yet turbulent, the KH billows develop strong buoyancy gradients where $\mathscr{M}$ is large. During this time, $\mathscr{P}_a$ is rapidly converted to background potential energy $\mathscr{P}_b$ (figure 15*d*,*e*). The dissipation rate is smaller than the mixing rate because the flow is not turbulent at this stage; hence the irreversible mixing efficiency η_i is greatest.

When the shear layer is close to the boundary (small d), the roll-up of the KH billows weakens, and SCI (§ 5.2) is therefore suppressed. Because of this, the first peak of $\mathscr{M}$ (e.g. red curve at $t = 140$ when $d = 3$ in figure 15*a*) is reduced. Boundary proximity also reduces dissipation during this time (figure 15*b*).

A precipitous drop in η_i occurs immediately after the first local maximum (figure 15*c*), due to the emergence of the 3-D secondary instabilities that collapse the KH billows. The value of $\langle \mathscr{K}_{3d} \rangle_{xyz}$ rapidly increases at this stage, e.g. $t \sim 140$–160 for $d = 10$ (figure 15*g*), suggesting the emergence of 3-D turbulence. Therefore, $\mathscr{P}_a$ (figure 15*d*) as well as $\langle \mathscr{K}_{2d} \rangle_{xz}$ (figure 15*f*) drop to a local minimum because the 2-D KH billow structure is partly destroyed. As a consequence, the instantaneous mixing efficiency decreases as $\mathscr{M}$ is reduced but ϵ simultaneously increases.

The second peak of $\mathscr{M}$ and η_i (e.g. at $t \sim 200$ for $d = 10$ in figure 15*a*) is associated with the turbulent stage of the flow evolution. The dissipation rate (figure 15*b*) reaches its maximum shortly after the maximum of $\mathscr{M}$. Pairing involves significant vertical motion and thus enhances $\mathscr{P}_a$ (e.g. $t = 150$–180 when $d = 10$ in figure 15*d*). Therefore, $\mathscr{P}_b$ and $\mathscr{M}$ both increase at $t = 180$. In contrast, the suppression of pairing by the boundary effect (e.g. $t = 200$ when $d = 3$ in figure 15*d*) reduces $\mathscr{P}_a$ as well as $\mathscr{P}_b$. As a result, mixing efficiency is reduced.

https://doi.org/10.1017/jfm.2023.412 Published online by Cambridge University Press

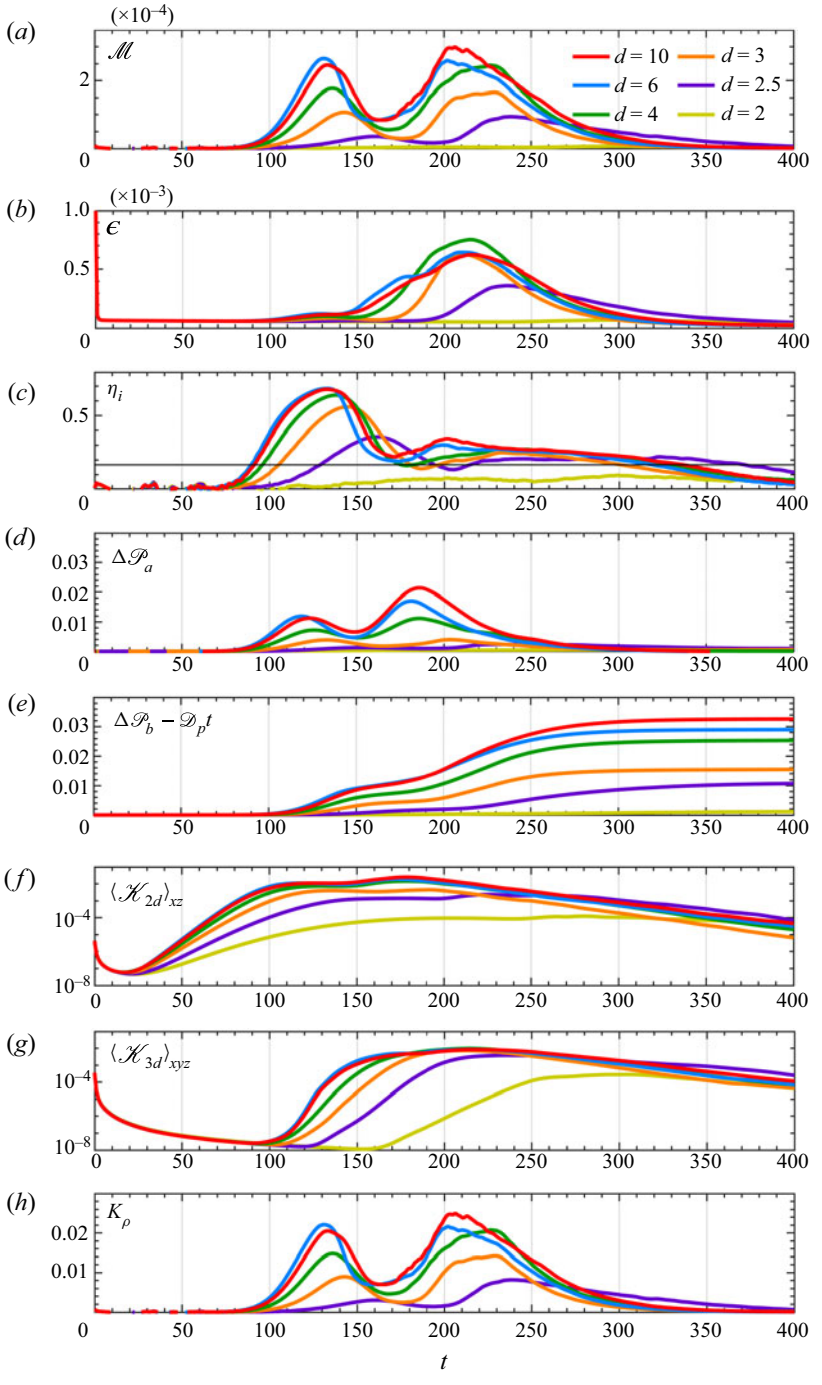

Figure 15. Time variation of (*a*) mixing rate, (*b*) total dissipation rate and (*c*) instantaneous mixing efficiency with different values of d. Horizontal line denotes the canonical value of $\eta_i \sim 1/6$. Time variation of changes from the initial state in (*d*) available potential energy $\mathscr{P}_a$, (*e*) background potential energy $\mathscr{P}_b$ associated with macroscopic motions. Volume-averaged (*f*) 2-D kinetic energy $\mathscr{K}_{2d}$, (*g*) 3-D kinetic energy $\mathscr{K}_{3d}$. (*h*) Turbulent diffusivity, K_ρ. All curves are ensemble averaged.

https://doi.org/10.1017/jfm.2023.412 Published online by Cambridge University Press

During the fully turbulent stage, the instantaneous mixing efficiency roughly converges to the canonical value of $\eta_i \sim 1/6$ or $\Gamma = 0.2$. In the post-turbulent stage, $\mathscr{M}$ drops to ~ 0 whereas the mean kinetic energy continues to dissipate. Therefore, η_i gradually decays to ~ 0.

We further relate the mixing efficiency to a turbulent diffusivity associated with irreversible mixing devised by Salehipour & Peltier (2015, their (2.23)). Using the present non-dimensionalization, this is

$$K_\rho = \Gamma \frac{Re_b}{Re_0}, \tag{6.1}$$

where Re_b is the buoyancy Reynolds number $\epsilon^*/\nu^* N^{*2}$. The time variation of K_ρ is shown in figure 15(*h*) with different values of d. The first peak of K_ρ is associated with the roll up of the KH billow, during which the mixing efficiency is maximum. The second peak is associated with turbulence, where ϵ and $\langle \mathscr{K}_{3d} \rangle_{xyz}$ are large. The value of K_ρ drops significantly with decreasing d as does the mixing rate.

We further demonstrate the importance of the route to turbulent mixing by showing the cumulative mixing, dissipation and mixing efficiency (2.19) for various values of d in figure 16. All three quantities decrease monotonically with decreasing d. The net mixing and dissipation vary slightly when $d \geqslant 4$, but drop sharply as $d < 4$ (figure 16*a*,*b*). This suggests that the impact of the boundary on mixing and dissipation becomes prominent when d is less than 4 due to the suppression of pairing and SCI. The abrupt decrease in cumulative mixing efficiency observed at $d < 4$ could be attributed to a combination of changes in net dissipation and mixing. We consider the derivative of the cumulative mixing efficiency with respect to d

$$\frac{1}{\eta_c}\frac{\partial \eta_c}{\partial d} = \frac{1}{\Gamma_c + 1}\left(\frac{1}{\mathscr{M}_c}\frac{\partial \mathscr{M}_c}{\partial d} - \frac{1}{\epsilon_c}\frac{\partial \epsilon_c}{\partial d}\right), \tag{6.2}$$

where the subscript 'c' refers to cumulative values. The boundary effect diminishes net dissipation (figure 16*a*, dotted line), leading to an increase in cumulative mixing efficiency ((6.2), second term in parentheses). However, it also diminishes net mixing, which is a key factor contributing to the sharp reduction in cumulative mixing efficiency when d is less than 4. Because the relative change in $\mathscr{M}_c$ is considerably greater than that in ϵ_c, i.e. $(1/\mathscr{M}_c)(\partial \mathscr{M}_c/\partial d) > (1/\epsilon_c)(\partial \epsilon_c/\partial d)$, the change in η_c is particularly pronounced.

For smaller d, e.g. $d = 2$, the net mixing $\int \mathscr{M}\, \mathrm{d}t$ is small, but the net dissipation persists since the dissipation of the mean flow is non-zero. Therefore, the efficiency of mixing is considerably reduced.

7. Summary and discussion

In geophysical flows, much of the most important shear-driven turbulent mixing appears near boundaries. Here, we have shown that boundary proximity significantly modifies the life cycle of turbulence in a stably stratified shear layer. A classical KH instability has been investigated by performing ensembles of DNS experiments with $Re_0 = 1000$, $Ri_0 = 0.12$ and $Pr = 1$. Absent boundary effects, the moderately low Ri_0 and Re_0 ensure the amalgamation of the KH billows. Our study describes the impact of boundary proximity on the primary KH instability, the subharmonic pairing instability, the 3-D secondary instability and the resulting turbulent mixing.

When the shear layer is close to the boundary, the primary KH billows are geometrically flatter. Furthermore, the evolution of the KH instability is extended over longer periods of time, so the transition to turbulence is delayed.

https://doi.org/10.1017/jfm.2023.412 Published online by Cambridge University Press

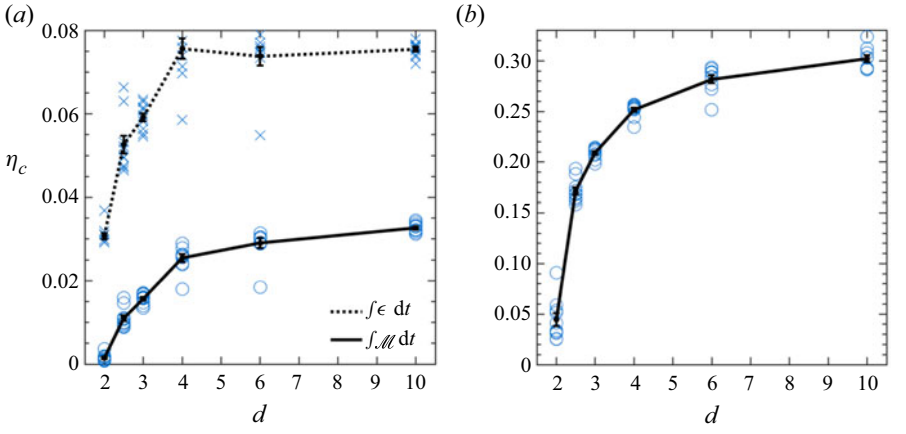

Figure 16. Cumulative (*a*) mixing (solid line) and dissipation (dotted line), and (*b*) mixing efficiencies calculated over an entire mixing event for different values of d. Error bars are standard error of the mean.

Mashayek & Peltier (2013) explained that when Re_0 is sufficiently large, the early emerging 3-D secondary instabilities can suppress pairing. Pairing would also be suppressed by gravity at higher Ri_0 (Smyth 2003; Mashayek & Peltier 2012*a*), and tends to be either unchanged or suppressed with an increase in Pr (Salehipour *et al.* 2015; Rahmani, Seymour & Lawrence 2016). Our study provides an additional explanation as to why pairing is rarely observed in geophysical flows. When the boundary effect is negligible, the linear phase speeds of the KH and subharmonic modes are virtually identical and equal to zero. When the shear layer is close to the boundary, on the other hand, the KH and subharmonic phase speeds diverge so that phase locking is prevented and pairing is therefore suppressed.

During the time when the primary KH instability is growing exponentially, CCI triggers 3-D motions in the cores of the billows. This is because the vortex at the central core tilts, resulting in energy extraction from the background shear via Reynolds stress. At this stage, CCI dominates for all boundary proximities.

When the boundary effect is negligible, SCI becomes the dominant 3-D secondary instability. The buoyancy production is greatly enhanced because unstable sublayers are formed within the billows. The boundary effect suppresses SCI because the roll up of the billows is counteracted by bottom drag. In contrast to the suppression of SCI, CCI remains dominant throughout the preturbulent stage. By forcing an alternate route for the transition of a 2- KH billow to 3-D turbulence, the boundary effect inevitably changes the resulting mixing.

The suppression of pairing weakens the conversion from $\mathscr{P}_a$ to $\mathscr{P}_b$ and reduces irreversible mixing. Although the suppression of pairing leads to a decline in dissipation, it is likely that dissipation near the boundary is amplified when d is smaller. Therefore, instantaneous mixing efficiency is reduced. Furthermore, the suppression of SCI by the boundary also diminishes the mixing rate and mixing efficiency. The cumulative irreversible mixing, dissipation and mixing efficiency, as well as turbulent diffusivity, decrease monotonically with decreasing distance from the shear layer to the boundary.

This study has been confined to a small subset of the continuum of initial states for practical reasons. Experiments with large Re_0 and Pr are expected to be affected by the boundary but the effect may manifest differently because the route to turbulent mixing is inherently different. Both the threshold value for d at which boundary effects become

https://doi.org/10.1017/jfm.2023.412 Published online by Cambridge University Press

strong and the onset time of 3-D secondary instability are expected to be sensitive to the value of the Reynolds number. As mentioned in § 4, Mashayek & Peltier (2013) show that 3-D secondary instability grows more rapidly when Re_0 is large, therefore, t_{3d} is expected to be smaller and pairing is, therefore, less likely. The effects of increasing Re_0 on t_{sub} and on the threshold value of d are subjects for future study.

The cores of the KH billows are referred to as 'quiet' in observations of the high-Re_0 and high-Pr flow of a salt-stratified estuary by Geyer *et al.* (2010). The DNS experiments have shown that, with large Re_0 and Pr, there is no density variance in the core of the billows but only in the periphery and the braid (Salehipour *et al.* 2015). This is potentially because the core of the billows is already well mixed due to previous 3-D secondary instability. In contrast, our results show that pairing and CCI play an important role during the evolution of the KH instability and the resulting mixing. A comprehensive understanding of the boundary effects on shear instability and the resulting turbulent mixing, particularly in the geophysical cases, will require the exploration of large Re_0 and Pr cases.

We have considered a classical KH instability to understand the boundary proximity effect. However, KH is not the only instability that may arise in a stratified shear flow. When buoyancy gradients are sufficiently sharp, the flow may be susceptible to the Holmboe instability (Holmboe 1962). Furthermore, flows with asymmetric background profiles may exhibit instabilities with a mixture of KH- and Holmboe-like behaviour (e.g. Carpenter, Lawrence & Smyth 2007; Yang, Tedford & Lawrence 2019; Olsthoorn, Kaminski & Robb 2023). Understanding how boundary proximity affects these processes may provide insights on future parameterizations of mixing in the ocean near boundaries. Studying beyond shear-driven turbulence and whether the alternative mechanisms have similar mixing properties may also be of future interest.

We note that the flow profiles considered here differ from real-world boundary layer flows in two key ways. The first is our choice of a hyperbolic–tangent shear and stratification. Classical turbulent boundary layer flows often exhibit logarithmic profiles with elevated shear at the boundary (e.g. Marusic *et al.* 2013; Bluteau *et al.* 2018), although the specific details of the flow vary with surface roughness, ambient stratification and external pressure gradients. While the profiles considered here differ from these classical boundary layers, we make this choice so as to facilitate comparison between our simulations and the isolated hyperbolic–tangent shear layer commonly studied in the KH literature. Secondly, the bottom boundary layer or the surface layer in the ocean is often turbulent. While the effect of boundary proximity on KH instability is pronounced, pre-existing turbulence should be taken into account for KH instabilities (Brucker & Sarkar 2007; Kaminski & Smyth 2019), especially near boundaries, where mixed layers are not initially laminar.

The flat bottom boundary is a simplification, as the real-world topography can be much more complex. Shear instability may occur near a ridge or a sloping topography. Internal waves may be generated near those boundaries, where the base flow may be altered and the boundary effect is not uniform. A nearby surface boundary, e.g. where the shear is created by wind stress in a diurnal warm layer (Hughes *et al.* 2021), can similarly reduce the growth rate of the instability. However, the frictional effect on the shear instability is smaller at the surface than at the bottom, as represented in our model by the free-slip top boundary (§ 2.1). We have shown that SCI is suppressed by a no-slip boundary because the boundary drag counteracts the roll up of the billows. Nonetheless, the no-slip condition results in higher dissipation near the boundary, potentially altering the evolution of the billows (Baglaenko 2016). With a free-slip boundary, however, no drag counteracts the roll-up process. Therefore, the suppression of SCI due to the free-slip boundary is expected

https://doi.org/10.1017/jfm.2023.412 Published online by Cambridge University Press

to be smaller. The effects of different boundary types (e.g. free slip, free surface) should be a focus for future research.

This study can potentially provide insights into future measurements near boundaries in the atmosphere and oceans. The dependence of mixing efficiency on boundary proximity can be estimated via microstructure measurements. Furthermore, acoustic backscatter measurements can delineate how the geometry of the KH billows varies with boundary proximity (e.g. Holleman *et al.* 2016; Tu *et al.* 2020).

While pairing is rarely detected in geophysical flows, the related phenomena called 'tubes' and 'knots' are commonly observed in the atmosphere (Thorpe 2002; Smyth & Moum 2012; Fritts *et al.* 2022). Tubes and knots arise when KH billow cores are misaligned. Unlike pairing in our study, knots often appear locally in the spanwise direction. Fritts *et al.* (2022) has found that the transition to turbulence is accelerated and turbulence is significantly stronger in tubes and knots than in other types of secondary instabilities (e.g. SCI). Future studies should address the effects of boundary proximity on tubes and knots. In particular, the question of whether boundary proximity suppresses tubes and knots by reducing the misalignment of the KH billow cores will be of interest.

Acknowledgements. This paper is part of the first author's PhD thesis at Oregon State University. We appreciate useful input from advisory committee members J. Moum, J. Liburdy, J. Nash and B. Pearson. We appreciate J. Taylor's work in creating and curating DIABLO. We acknowledge high-performance computing support on Cheyenne (doi:10.5065/D6RX99HX) provided by NCAR's Computational and Information Systems Laboratory, sponsored by the US National Science Foundation.

Funding. This work was funded by the US National Science Foundation under grant OCE-1830071. A.K.K. was supported as the Ho-Shang and Mei-Li Lee Faculty Fellow in Mechanical Engineering at UC Berkeley.

Declaration of interests. The authors report no conflict of interest.

Data availability statement. DIABLO is available at https://github.com/johnryantaylor/DIABLO. Output data are available by request to the authors.

Author ORCIDs.
Chih-Lun Liu https://orcid.org/0000-0001-5134-7993;
Alexis K. Kaminski https://orcid.org/0000-0002-4838-2453;
William D. Smyth https://orcid.org/0000-0001-5505-2009.

References

Armi, L. & Mayr, G.J. 2011 The descending stratified flow and internal hydraulic jump in the lee of the Sierras. *J. Appl. Meteorol. Clim.* **50** (10), 1995–2011.

Baglaenko, A. 2016 The effects of confinement on Kelvin–Helmholtz billows. PhD thesis, University of Waterloo, ON.

Bluteau, C.E., Ivey, G.N., Donis, D. & McGinnis, D.F. 2018 Determining near-bottom fluxes of passive tracers in aquatic environments. *Geophys. Res. Lett.* **45** (6), 2716–2725.

Brucker, K. & Sarkar, S. 2007 Evolution of an initially turbulent stratified shear layer. *Phys. Fluids* **19**, 105105.

Carpenter, J.R., Lawrence, G.A. & Smyth, W.D. 2007 Evolution and mixing of asymmetric Holmboe instabilities. *J. Fluid Mech.* **582**, 103–132.

Caulfield, C.P. 2021 Layering, instabilities, and mixing in turbulent stratified flows. *Annu. Rev. Fluid Mech.* **53** (1), 113–145.

Caulfield, C.P. & Peltier, W.R. 2000 The anatomy of the mixing transition in homogeneous and stratified free shear layers. *J. Fluid Mech.* **413**, 1–47.

Chang, M.-H., *et al.* 2022 Internal hydraulic transition and turbulent mixing observed in the Kuroshio over the I-Lan ridge off Northeastern Taiwan. *J. Phys. Oceanogr.* **52** (12), 3179–3198.

Chang, M.-H., Jheng, S.-Y. & Lien, R.-C. 2016 Trains of large Kelvin–Helmholtz billows observed in the Kuroshio above a seamount. *Geophys. Res. Lett.* **43** (16), 8654–8661.

https://doi.org/10.1017/jfm.2023.412 Published online by Cambridge University Press

CORCOS, G.M. & SHERMAN, F.S. 1976 Vorticity concentration and the dynamics of unstable free shear layers. *J. Fluid Mech.* **73**, 241–264.

DAVIS, P.A. & PELTIER, W.R. 1979 Some characteristics of the Kelvin–Helmholtz and resonant overreflection modes of shear flow instability and of their interaction through vortex pairing. *J. Atmos. Sci.* **36** (12), 2394–2412.

DONG, W., TEDFORD, E.W., RAHMANI, M. & LAWRENCE, G.A. 2019 Sensitivity of vortex pairing and mixing to initial perturbations in stratified shear flows. *Phys. Rev. Fluids* **4**, 063902.

FRITTS, D.C., WANG, L., LUND, T.S. & THORPE, S.A. 2022 Multi-scale dynamics of Kelvin–Helmholtz instabilities. Part 1. Secondary instabilities and the dynamics of tubes and knots. *J. Fluid Mech.* **941**, A30.

FUKAO, S., LUCE, H., MEGA, T. & YAMAMOTO, M.K. 2011 Extensive studies of large-amplitude Kelvin–Helmholtz billows in the lower atmosphere with VHF middle and upper atmosphere radar. *Q. J. R. Meteorol. Soc.* **137** (657), 1019–1041.

GEYER, W.R., LAVERY, A., SCULLY, M.E. & TROWBRIDGE, J.H. 2010 Mixing by shear instability at high Reynolds number. *Geophys. Res. Lett.* **37**, L22607.

GREGG, M.C., D'ASARO, E.A., RILEY, J.J. & KUNZE, E. 2018 Mixing efficiency in the ocean. *Annu. Rev. Marine Sci.* **10** (1), 443–473.

GUHA, A. & RAHMANI, M. 2019 Predicting vortex merging and ensuing turbulence characteristics in shear layers from initial conditions. *J. Fluid Mech.* **878**, R4.

HOLLEMAN, R.C., GEYER, W.R. & RALSTON, D.K. 2016 Stratified turbulence and mixing efficiency in a salt wedge estuary. *J. Phys. Oceanogr.* **46**, 1769–1783.

HOLMBOE, J. 1962 On the behaviour of symmetric waves in stratified shear layers. *Geophys. Publ.* **24**, 67–113.

HOLT, J.T. 1998 Experiments on Kelvin–Helmholtz billows influenced by boundaries. *Geophys. Astrophys. Fluid Dyn.* **89** (3–4), 205–233.

HOWARD, L.N. 1961 Note on a paper of John W. Miles. *J. Fluid Mech.* **10**, 509–512.

HUGHES, K.G., MOUM, J.N., SHROYER, E.L. & SMYTH, W.D. 2021 Stratified shear instabilities in diurnal warm layers. *J. Phys. Oceanogr.* **51** (8), 2583–2598.

IVEY, G.N., WINTERS, K.B. & KOSEFF, J.R. 2008 Density stratification, turbulence, but how much mixing? *Annu. Rev. Fluid Mech.* **40** (1), 169–184.

KAMINSKI, A.K. & SMYTH, W.D. 2019 Stratified shear instability in a field of pre-existing turbulence. *J. Fluid Mech.* **863**, 639–658.

KLAASSEN, G.P. & PELTIER, W.R. 1985*a* The evolution of finite-amplitude Kelvin–Helmholtz billows in two spatial dimensions. *J. Atmos. Sci.* **42**, 1321–1339.

KLAASSEN, G.P. & PELTIER, W.R. 1985*b* The onset of turbulence in finite-amplitude Kelvin–Helmholtz billows. *J. Fluid Mech.* **155**, 1–35.

KLAASSEN, G.P. & PELTIER, W.R. 1989 The role of transverse secondary instabilities in the evolution of free shear layers. *J. Fluid Mech.* **202**, 367–402.

KLAASSEN, G.P. & PELTIER, W.R. 1991 The influence of stratification on secondary instability in free shear layers. *J. Fluid Mech.* **227**, 71–106.

LEWIN, S.F. & CAULFIELD, C.P. 2021 The influence of far-field stratification on turbulent mixing. *J. Fluid Mech.* **928**, A20.

LIU, C.-L., KAMINSKI, A.K. & SMYTH, W.D. 2022 The butterfly effect and the transition to turbulence in a stratified shear layer. *J. Fluid Mech.* **953**, A43.

MARUSIC, I., MONTY, J.P., HULTMARK, M. & SMITS, A.J. 2013 On the logarithmic region in wall turbulence. *J. Fluid Mech.* **716**, R3.

MASHAYEK, A. & PELTIER, W.R. 2011 Three-dimensionalization of the stratified mixing layer at high Reynolds number. *Phys. Fluids* **23** (11), 111701.

MASHAYEK, A. & PELTIER, W.R. 2012*a* The 'zoo' of secondary instabilities precursory to stratified shear flow transition. Part 1. Shear aligned convection, pairing, and braid instabilities. *J. Fluid Mech.* **708**, 5–44.

MASHAYEK, A. & PELTIER, W.R. 2012*b* The 'zoo' secondary instabilities precursory to stratified shear flow transition. Part 2. The influence of stratification. *J. Fluid Mech.* **708**, 45–70.

MASHAYEK, A. & PELTIER, W.R. 2013 Shear-induced mixing in geophysical flows: does the route to turbulence matter to its efficiency? *J. Fluid Mech.* **725**, 216–261.

MAYOR, S.D. 2017 Observations of microscale internal gravity waves in very stable atmospheric boundary layers over an orchard canopy. *Agr. Forest Meterol.* **244–245**, 136–150.

MILES, J.W. 1961 On the stability of heterogeneous shear flows. *J. Fluid Mech.* **10**, 496–508.

MOUM, J.N., NASH, J.D. & SMYTH, W.D. 2011 Narrowband, high-frequency oscillations in the upper equatorial ocean. Part 1: intepretation as shear instabilities. *J. Phys. Oceanogr.* **41**, 397–411.

MUNK, W.H. & WUNCH, C. 1998 Abyssal recipes II: energetics of tidal and wind mixing. *Deep-Sea Res.* **45**, 1977–2010.

https://doi.org/10.1017/jfm.2023.412 Published online by Cambridge University Press

OLSTHOORN, J., KAMINSKI, A.K. & ROBB, D.M. 2023 Dynamics of asymmetric stratified shear instabilities. *Phys. Rev. Fluids* **8** (2), 024501.

OSBORN, T.R. 1980 Estimates of the local rate of vertical diffusion from dissipation measurements. *J. Phys. Oceanogr.* **10**, 83–89.

PELTIER, W.R. & CAULFIELD, C.P. 2003 Mixing efficiency in stratified shear flows. *Annu. Rev. Fluid Mech.* **35**, 136–167.

RAHMANI, M., LAWRENCE, G.A. & SEYMOUR, B.R. 2014 The effect of Reynolds number on mixing in Kelvin–Helmholtz billows. *J. Fluid Mech.* **759**, 612–641.

RAHMANI, M., SEYMOUR, B.R. & LAWRENCE, G.A. 2016 The effect of Prandtl number on mixing in low Reynolds number Kelvin–Helmholtz billows. *Phys. Fluids* **28** (5), 054107.

SALEHIPOUR, H. & PELTIER, W.R. 2015 Diapycnal diffusivity, turbulent Prandtl number and mixing efficiency in Boussinesq stratified turbulence. *J. Fluid Mech.* **775**, 464–500.

SALEHIPOUR, H., PELTIER, W.R. & MASHAYEK, A. 2015 Turbulent diapycnal mixing in stratified shear flows: the influence of Prandtl number on mixing efficiency and transition at high Reynolds number. *J. Fluid Mech.* **773**, 178–223.

SMYTH, W.D., MAYOR, S.D. & LIAN, Q. 2023 The role of ambient turbulence in canopy wave generation by Kelvin–Helmholtz instability. *Boundary-Layer Meteorol.* **187**, 501–526.

SMYTH, W.D. 2003 Secondary Kelvin–Helmholtz instability in a weakly stratified shear flow. *J. Fluid Mech.* **497**, 67–98.

SMYTH, W.D. 2006 Secondary circulations in Holmboe waves. *Phys. Fluids* **18**, 06414.

SMYTH, W.D. & CARPENTER, J.R. 2019 *Instability in Geophysical Flows*. Cambridge University Press.

SMYTH, W.D. & MOUM, J.N. 2000 Length scales of turbulence in stably stratified mixing layers. *Phys. Fluids* **12**, 1327–1342.

SMYTH, W.D. & MOUM, J.N. 2012 Ocean mixing by Kelvin–Helmholtz instability. *Oceanography* **5**, 140–149.

SMYTH, W.D., MOUM, J.N., LI, L. & THORPE, S.A. 2013 Diurnal shear instability, the descent of the surface shear layer, and the deep cycle of equatorial turbulence. *J. Phys. Oceanogr.* **43**, 2432–2455.

SMYTH, W.D. & PELTIER, W.R. 1993 Two-dimensional turbulence in homogeneous and stratified shear layers. *Geophys. Astrophys. Fluid Dyn.* **69**, 1–32.

TAYLOR, J.R. 2008 *Numerical Simulations of the Stratified Oceanic Bottom Boundary Layer*. University of California.

THORPE, S.A. 2002 The axial coherence of Kelvin–Helmholtz billows. *Q. J. R. Meteorol. Soc.* **128**, 1529–1542.

TSENG, Y.-H. & FERZIGER, J.H. 2001 Mixing and available potential energy in stratified flows. *Phys. Fluids* **13** (5), 1281–1293.

TU, J., FAN, D., LIAN, Q., LIU, Z., LIU, W., KAMINSKI, A. & SMYTH, W. 2020 Acoustic observations of Kelvin–Helmholtz billows on an estuarine lutocline. *J. Geophys. Res.: Oceans* **125** (4), e2019JC015383.

TU, J., FAN, D., LIU, Z. & SMYTH, W. 2022 Scaling the mixing efficiency of sediment-stratified turbulence. *Geophys. Res. Lett.* **49** (13), e2022GL099025.

VAN HAREN, H. & GOSTIAUX, L. 2010 A deep-ocean Kelvin–Helmholtz billow train. *Geophys. Res. Lett.* **37**, L03605.

VAN HAREN, H., GOSTIAUX, L., MOROZOV, E. & TARAKANOV, R. 2014 Extremely long Kelvin–Helmholtz billow trains in the Romanche Fracture Zone. *Geophys. Res. Lett.* **41**, 8445–8451.

VANDINE, A., PHAM, H.T. & SARKAR, S. 2021 Turbulent shear layers in a uniformly stratified background: DNS at high Reynolds number. *J. Fluid Mech.* **916**, A42.

WINTERS, K., LOMBARD, P.N., RILEY, J.J. & D'ASARO, E.A. 1995 Available potential energy and mixing in density-stratified fluids. *J. Fluid Mech.* **289**, 115–128.

WUNSCH, C. & FERRARI, R. 2004 Vertical mixing, energy, and the general circulation of the oceans. *Annu. Rev. Fluid Mech.* **36** (1), 281–314.

YANG, A.J.K., TEDFORD, E.W. & LAWRENCE, G.A. 2019 The spatial evolution of velocity and density profiles in an arrested salt wedge. *Theor. Appl. Mech. Lett.* **9** (6), 403–408.

https://doi.org/10.1017/jfm.2023.412 Published online by Cambridge University Press